2014

THE EFFECTS OF SEA ICE ON GAS TRANSFER VELOCITIES AND GAS PARTITIONING BETWEEN WATER AND SEA ICE

Ann Lovely
University of Rhode Island, alovely424@gmail.com

THE EFFECTS OF SEA ICE ON GAS TRANSFER VELOCITIES AND GAS PARTITIONING BETWEEN WATER AND SEA ICE

BY

ANN LOVELY

A THESIS SUBMITTED IN PARTIAL FULFILLMENT OF THE REQUIREMENTS FOR THE DEGREE OF

MASTER OF SCIENCE

IN

OCEANOGRAPHY

UNIVERSITY OF RHODE ISLAND

2014

MASTER OF SCIENCE THESIS

OF

ANN LOVELY

APPROVED:

Thesis Committee:
Major Professor: Brice Loose

Chris Kincaid

Jason Dahl

Nasser H. Zawia
DEAN OF THE GRADUATE SCHOOL

UNIVERSITY OF RHODE ISLAND
2014

ABSTRACT

Sea ice is a defining feature of the polar geochemical ecosystem. It is a critical substrate for marine biota and it regulates ocean-atmosphere exchange, including the exchange of biogenic gases such as CO_2 and CH_4. In this study, we are concerned with determining the rates and pathways that govern gas transport around sea ice. N_2O, SF_6 and ^3He were used as inert tracers of the transport and exchange processes taking place between the water, ice and air in a laboratory sea ice experiment. Using gas budgets and gradients we were able to estimate these transport rates as a function of both water current speed and wind speed. We observed divergence in the mass balance of each gas, but most of these patterns follow consistent behavior based on differences in gas solubility and molecular diffusivity as well as the molecular size of each gas. Diffusive flux of the gases into the ice was found to be on the scale of 10^{-6} $cm^2\ s^{-1}$, which is nearly the same as molecular diffusion in water and too slow to be of consequence for air-sea gas transport. In contrast, we observed increasing trends in the air-sea gas transfer velocities (k_{eff}) as a function of increased forcing. Gas transfer rates responded positively to both wind and water current speed as well as the combination of the two, indicating that gas transfer cannot be uniquely predicted by wind speed alone in the presence of sea ice.

ACKNOWLEDGEMENTS

I would like to thank my advisor, Brice Loose, for all of his support over the last two years. I could not have achieved this without him! I would also like to thank all of my co-authors at the Lamont-Doherty Earth Observatory of Columbia University: Peter Schlosser, Wade McGillis, and Chris Zappa, for their support through the process and help with the lab work at CREEL. Thanks also to Peter and his lab at LDEO for running all of the helium samples. Diana Hsueh, Scott Brown and Tom Morrell, your help and company at CRREL and your assistance with questions since then is much appreciated. I would also like to thank CRREL, my co-author from there: Don Perovich, and everyone else there who made this work possible, especially Leonard Zabilansky, Bruce Elder and Gordon Gooch. Thanks to Dennis Graham at URI GSO for running some of our samples for DIC and alkalinity.

A special thanks to all of my friends and family for their love and support over the last two years. Thanks for putting up with me! CACS second floor, you guys are the best!

Finally I would like to thank the NSF-OPP for their funding of the GAPS experiment and URI and Tabor Academy for supporting me over the last two years.

PREFACE

This thesis is written in the format of a manuscript, *The effects of sea ice on gas transfer velocities and gas partitioning between water and sea ice*, being prepared for publication in the journal *Ocean Science*. It is co-authored by Brice Loose, Peter Schlosser, Don Perovich, Wade McGillis and Chris Zappa.

TABLE OF CONTENTS

LIST OF TABLES

LIST OF FIGURES

MANUSCRIPT 1

The effects of sea ice on gas transfer velocities and gas partitioning between water and sea ice

by

A. Lovely[1], B. Loose[1], W. McGillis[2], D. Perovich[3], C. Zappa[2], S. Brown[2], T. Morell[2], D. Hsueh[2], P. Schlosser[2,4,5]

In preparation for submission to Ocean Science

[1] Graduate School of Oceanography, University of Rhode Island, 215 South Ferry Rd., Narragansett, RI, 02882, USA
[2] Lamont-Doherty Earth Observatory of Columbia University, 61 Rout 9W, Palisades, NY 10964, USA
[3] US Army Corps of Engineers Cold Regions Research and Engineering Laboratory, 72 Lyme Rd., Hanover, NH, 03755, USA
[4] Department of Earth and Environmental Sciences, Columbia University, Room 106 Geosciences Bldg., Palisades, NY 10964, USA
[5] Department of Earth and Environmental Engineering, Columbia University, 918 Seeley Mudd Bldg., 500 West 120th St, New York, NY 10027, USA

Abstract

Sea ice is a defining feature of the polar geochemical ecosystem. It is a critical substrate for marine biota and it regulates ocean-atmosphere exchange, including the exchange of biogenic gases such as CO_2 and CH_4. In this study, we are concerned with determining the rates and pathways that govern gas transport around sea ice. N_2O, SF_6 and ^3He were used as inert tracers of the transport and exchange processes taking place between the water, ice and air in a laboratory sea ice experiment. Using gas budgets and gradients we were able to estimate these transport rates as a function of both water current speed and wind speed. We observed divergence in the mass balance of each gas, but most of these patterns follow consistent behavior based on differences in gas solubility and molecular diffusivity as well as the molecular size of each gas. Diffusive flux of the gases into the ice was found to be on the scale of 10^{-6} $cm^2\ s^{-1}$, which is nearly the same as molecular diffusion in water and too slow to be of consequence for air-sea gas transport. In contrast, we observed increasing trends in the air-sea gas transfer velocities (k_{eff}) as a function of increased forcing. Gas transfer rates responded positively to both wind and water current speed as well as the combination of the two, indicating that gas transfer cannot be uniquely predicted by wind speed alone in the presence of sea ice.

1.1. INTRODUCTION

The burning of fossil fuels is causing the concentration of anthropogenic carbon dioxide (CO_2) in the atmosphere to increase at an unprecedented rate. Approximately one third of this CO_2 ends up in the world's oceans (Khatiwala et al.,

2012) with the Southern Ocean (SO) being the most important conduit (Khatiwala et al., 2009). In the SO, 19.4 million km^2 (about 40%) of the ocean surface area south of 50°S is covered with ice during the austral winter (NSIDC). This is thought to represent a large barrier to air-sea exchange. But, it occurs during a time when the mixed layer reaches its deepest depths enabling a larger volume of water to interact with the surface ocean than during other seasons. The combination of these factors determines the net flux of gases between the atmosphere and ocean in the SIZ and may also impact the amount of CO_2 transported into and out of the deep ocean (Takahashi et al., 2009). Meanwhile, the SIZ of the Arctic Ocean is changing as the advance-retreat of the ice edge increases almost yearly. From 1979 to March 2014, sea ice extent in the Arctic shows a negative trend for every month (NSIDC). September has experienced the greatest loss; from 1979 to 2013 there has been a 14% per decade (40% overall) reduction in September sea ice extent (Stroeve et al., 2014). This increase in sea ice melt is resulting in an increase in the spring bloom and, thus, an increase in CO_2 uptake. It is also resulting in greater stratification, a scenario that could impact the flux and gas transfer velocities of important biogenic gases like O_2, CO_2 and dimethylsulfide (DMS).

In the fall and winter, the formation of sea ice leads to deep-water formation and, with it, the sequestration of CO_2 that dissolved into the dense water when it was in contact with the atmosphere (Omar et al., 2005). The cold temperatures act to enhance the solubility of gases in these water masses enabling greater CO_2 absorbance than would occur at lower latitudes in the surface ocean (Weiss, 1974). In the southern hemisphere, isopycnals of the deep ocean outcrop in this region, bringing

deep water to the surface where it interacts with the atmosphere releasing deep ocean CO_2. These processes, combined yet opposing, result in the polar oceans playing a central role in the global carbon cycle and in the oceans ability to act as a carbon sink (Caldeira and Duffy, 2000; Marinov et al., 2006).

There is a lot of uncertainty regarding the amount of CO_2 actually sequestered in these processes and the net amount absorbed by the SO has been revised many times through the years. Takahashi et al. (1997) reported it at 1 Pg C yr^{-1} and then McNeil et al. (2007) reported it as 0.4 Pg C yr^{-1} before Takahashi et al. (2009) revised their number to 0.04 Pg C yr^{-1}. This is in part due to the SO being one of the most poorly sampled oceanic regions with respect to CO_2 (Monteiro et al., 2010) even though it is one of the most important. The revisions to this important value reflect the difficulty of appropriately estimating gas exchange and primary production in the Southern Ocean and its sea ice zone. Here, we focus on the rate of air-sea gas exchange.

Gases enter and exit the ocean at the air-sea interface. A complete understanding of the rate of this flux and the potential effects of climate change on this rate are necessary to determine the future of the polar ocean as a carbon sink. Most estimates of gas transfer velocity (*k)* have relied on a wind-speed parameterization (e.g. Wanninkhof, 1992), which was built for the open ocean with mature wave fields. This method uses a quadratic relationship between wind speed (*U*) and *k* (Else et al., 2011; Wanninkhof et al., 2009). In sea ice covered regions, the practice has been to scale a windspeed-derived estimate of *k* by the fraction of open water (*f*) (Arrigo and van Dijken, 2007; Stephens and Keeling, 2000; Takahashi et al., 2009). However, this

approach, while simple and logical, is not based upon field or model estimates of k in sea ice and there is some evidence that it is not a good representation. In fact, the relationship between wind speed and turbulence may diminish as fetch is reduced while other processes such as current shear between the water and ice may dominate (McPhee, 1992). Sea ice can be permeable to gases (Golden, 2001; Gosink et al., 1976) so ventilation from sea ice covered waters can be a result of flux through the ice (k_{ice}) or open water (k). Therefore, we need to define a third k, k_{eff}, where

$$k_{eff}=(1-f)k_{ice}+(f)k \quad (1)$$

and (1-f) is the fraction of sea ice covered water. Methods using tracers to determine flux, such as the radon deficit method, the dual tracer method and tracer mass balance (used here) estimate k_{eff} while those using covariance flux or the gradient flux method yield k or k_{ice} as they work on a much smaller scale (Loose et al., 2014).

At this time there have only been two field studies of gas transfer in the presence of sea ice. Fanning and Torres (1991) estimated a k_{eff} in the Barents Sea using the ^{222}Rn deficit method during a period of over 90% ice cover (late winter) and during a period of ≤ 70% ice cover (late summer). This resulted in k_{600} (gas transfer velocity normalized to a Schmidt number, the ratio of viscosity to mass diffusivity, of 600) ranging from 1.44-3.6 m day^{-1} in late winter and 2.16-6.24 m day^{-1} in late summer. Rutgers van der Loeff et al. (2014) also used the radon deficit method to measure gas transfer velocities at both ice-covered and ice-free stations in the Arctic Ocean. At the stations with 100% open water their gas exchange measurements were in close agreement with those calculated using wind speed. Very little (<0.1 m day^{-1}), if any, gas exchange was measured at the ice-covered stations.

Modeling studies have also been undertaken to determine gas transfer velocities in the presence of sea ice. Takahashi et al. (2009) used Wanninkhof's (1992) wind parameterization to determine a mean k_{eff} for the ice-free SIZ of 3.6 m day^{-1} scaled by f derived from reanalysis of sea ice cover. Assuming that $f \geq 0.1$, they assert that k_{eff} is always ≥ 0.36 m day^{-1}. This is quite a bit smaller than the numbers presented by Fanning and Torres (1991) but larger than that presented by Rutgers van der Loeff et al. (2014). A study by Loose and Schlosser (2011) uses salinity, helium-3 and CFC-11 data collected from Ice Station Weddell to determine a k_{eff} of 0.11 m day^{-1} during May 1992, a time of almost 100% ice cover. This value indicates that exchange continues to occur in the limiting sea ice condition, suggesting that some open water remains scattered throughout the ice pack. Unfortunately the constraints on ice cover are not well enough defined to formulate a scaling relationship from this data, supporting the conclusion that gas exchange in sea ice covered water is largely unconstrained by data (Loose et al., 2011).

In laboratory experiments, Loose et al. (2009) found that the measured k_{eff} were consistently greater than those expected from a linear scaling between 100% open water and complete ice cover. They theorize this is a result of turbulence and circulation under the ice, although it may also be due to dynamic fluxes through the sea ice (Vancoppenolle et al., 2013). Morison et al. (1992) describe this process of under ice circulation as resulting in a renewal of water exposed in leads (ice-free zones), allowing for the portion of water interacting with the atmosphere to be greater than is indicated by the fraction of open water. Else et al. (2011) propose that this increase in gas transfer is due to increased turbulence resulting from brine rejection

during rapid cooling and, for CO_2, a modification of the carbonate system. None of these studies can conclusively and in detail explain the chemical and physical processes that cause the enhanced exchange (Else et al., 2011).

The penetrability of the sea ice microstructure to diffusion by gases is another area of question. Gosink et al. (1976) found that sea ice is permeable to gases at all temperatures, especially above -10°C, and they report a diffusivity (D) ranging from D=10^{-7} to 10^{-5} cm^2 s^{-1}. Loose et al. (2011) looked at the diffusivity of SF_6 and O_2 across sea ice at different laboratory conditions. They report higher values for D in the range of 10^{-4} to 10^{-5} cm^2 s^{-1}. This wide-ranging diffusivity may be a result of the many processes that govern the dynamics of gases within sea ice and its flux between the water and ice. This includes the porosity of sea ice, a property explored by Cox and Weeks (1983). They determined that much of the porosity is a function of the gas and brine volume in the ice and derived equations from which these two volumes can be determined using knowledge of ice salinity, temperature and density. This agrees with Bortkovskii's (2012) finding that the pores within sea ice are connected resulting in there being continuous channels within a united system. Gas bubbles have also been reported to nucleate and dissolve within the ice as temperatures change, advect within brine channels, rise vertically due to buoyancy, and nucleate as free gas during biogeochemical processes (Moreau et al., 2014). Despite these revelations sea ice continues to be treated as an impermeable barrier, yet sea ice microstructure and the dynamics of gases within it could greatly affect air-sea gas interactions in the SIZ (Loose et al., 2011).

Here we will explore the flux of gases across the ice-water interface as well as within sea ice. After correcting for the diffusive flux within the ice, we will attempt to connect the processes that produce turbulence around sea ice with the rate of gas exchange across the air-sea interface. This is done in a large-scale laboratory experiment in which the fraction of open water, water current, wind speed and air-water temperature gradient are all controlled. Values for D are determined using numerical methods and then k_{eff} is determined for different conditions of fraction open water, water current and wind speed.

1.2. Methods

1.2.1. Experiment setup and analytical measurements

The GAPS (Gas Transfer through Polar Sea ice) experiment was conducted in the Engineering Test Basin at the US Army Corp of Engineers Cold Regions Research and Engineering Lab (CRREL) in Hanover, NH. This is a 36x9x3m pool located in a temperature-controlled room that can reach temperatures as low as -29°C. Along one side a 20x2m wind tunnel was constructed containing a steel belt-drive ducted fan with a maximum rated flow of 430 m^3 min^{-1} that blew air through a flow straightener and along the water surface through the length of the wind tunnel. Four submersible impeller pumps powered by ½ HP 460V 3-phase motors produced a maximum flow rate of 7 m^3 min^{-1}. The pumps were placed at the western end of the tunnel to circulate the water through the test basin in the same direction as the wind (Figure **1**, Figure **2**). The fan and pumps were run on separate variable frequency drives and could be set to run at any frequency between 0 and 60 Hz, which has the effect of modulating their speed.

Measurement of the wind speed inside the tunnel was done using a Vaisala WS425 and Vaisala WMT700, both of which were suspended over the test basin from the roof of the wind tunnel. Three Nortek Aquadopp Profilers, instruments for measuring profiles of both horizontal and vertical velocity, were placed in the channel 0.85 m off the bottom (1.05 m below the water surface) looking upwards at the water surface, which was intermittently ice covered. Each sampled at 2 Hz for a 20-minute period every hour over which the profiles were averaged.

A CTD was mounted in the test basin to track salinity and temperature changes within the basin and an array of thermistor sensors was deployed along the outer edge of the wind tunnel ranging from 10 cm above the future ice surface to 60 cm below this point. The test basin was filled with tap water and 20 tons of 98% pure sodium chloride. Air was bubbled into the water to help dissolve the salt and the conductivity sensor on the CTD was used to check the salinity against that calculated to make sure all of the salt dissolved. Salt dissolution and brine rejection from the ice during freezing combined to bring the salinity to approximately 27.5 ppt when the experiment began (Figure 3). Although this salinity is lower than that of the ocean, it is great enough so there is no temperature-driven density inversion and the freezing point of the water is -1.55 °C. Time constraints and a fear that some salt would not dissolve resulted in our not adding more salt to raise the salinity to that of the polar oceans.

Before the surface of the test basin was frozen, a large amount of CO_2 was bubbled directly into the salt water to increase its concentration to over 15,000 ppm (Figure **4**). The test basin was then frozen to an ice thickness of 8.5 cm over 4.75 days. During this freezing event the surface of the wind tunnel was covered with Styrofoam

to keep it ice-free. This resulted in a 20 m lead and 91% ice cover. A total of 8.21 moles N_2O and $2.23x10^{-4}$ moles SF_6 were diffused into a gas-tight 500-gallon tank and, at the completion of freezing (day 2.5), this water was added to the test basin. On day 3.5, $1.83x10^{-6}$ moles ^3He were added to the test basin as a third tracer gas (Figure **4**). In this way, these three gas tracers were added beneath the ice without introducing tracer into the ice matrix itself and without producing bubbles that would be trapped beneath the ice. During each addition, the water pumps were set to their maximum speed to mix the gases through the entire test basin. Multiple scenarios of varying pump and wind speed were run (Table **1**). These are the 'long lead scenarios.'

A second freezing event began on day 15 to shorten the lead to 5 m and 96% ice cover, 18.5 cm thick. Salinity increased from 27.75 to 28.7 ppt (Figure 3). CO_2 was again bubbled directly into the test basin before freezing raising its concentration to about 14,000 ppm (Figure **4**). Multiple "forcing" scenarios, where gas exchange was induced by the production of turbulence from the pumps or fan, were completed (Table **1**). These are the 'short lead scenarios.'

1.2.2. Gas tracer sampling and analysis

To sample test basin water and determine the concentration of each tracer gas throughout the experiment, a 12V Rule-360 submersible pump was installed in the test basin channel (Figure **2**) 145 cm off the bottom (45 cm below the water surface). Vinyl tubing was attached to the pump to create a water sampling loop that ran from the test basin into the adjacent laboratory and back to the basin. A three-way valve set-up in the lab allowed water samples to be taken for N_2O, SF_6, ^3He and DIC/alkalinity analysis.

To measure N_2O and SF_6, 20 mL water samples were collected in 50 mL glass syringes. Approximately 30 mL of nitrogen was added to each syringe before samples equilibrated to room temperature and were then shaken for 10 minutes to expel any remaining gas from the water (Wanninkhof et al., 1987). The gaseous samples were injected into an SRI-8610C Gas Chromatograph with an Electron Capture Detector (GC-ECD). The concentration of SF_6 and N_2O in each sample was determined using Wanninkhof et al.'s (1987) headspace method. This method uses the peak area determined from the GC-ECD, the peak area of known standards (100ppmv N_2O, 10ppbv SF_6 and 1ppmv N_2O, 150 pptv SF_6 made by Scott Marrin, Riverside, CA), the volume of water sampled and the volume of gas injected into the GC-ECD. Tracer conservation, Henry's Law and the Ideal Gas Law are invoked to determine the concentration of tracer in the water (C_w) as

$$C_w = X\left(H + \frac{P}{RT} * \frac{V_a}{V_w}\right) \qquad (2)$$

where X is determined by multiplying the measured peak area by the predetermined calibration factor, H is Henry's Law Constant (accounts for the solubility of the gas at the given temperature and salinity), P is atmospheric pressure, R is the ideal gas constant, T is temperature, V_a is the volume of gas in the syringe and V_w is the volume of water in the syringe.

Samples for ^3He analysis were taken in copper tubes and sent to Lamont-Doherty Earth Institute of Columbia University for analysis on the Helium-Neon mass spectrometer which uses a VG5400 mass-spectrometer for helium isotope analysis and a Pfeiffer PrismaPlus quadrupole mass-spectrometer for analysis of neon isotopes. Analysis of these samples provided us with ^4He and Ne data as well. ^3He samples

were measured as $\delta^3 He$ and converted to mol m^{-3} (Torgersen et al., 1977). The measured concentration of the tracer gases throughout the experiment is shown in Figure **4** and Figure **5**.

After samples for ^3He, SF_6 and N_2O analysis were taken, the remaining water removed from the test basin was degassed in a membrane contactor and the gas in it was sent to a LICOR LI-840A CO_2/H_2O analyzer for pCO_2 analysis. This occurred continuously and after equilibration the water returned to the test basin. Water samples were also taken every 4 hours to monitor DIC and alkalinity in the test basin. Respiration in these samples was inactivated with mercuric chloride and samples were stored in sealed jars for later analysis at the University of Rhode Island.

Air samples taken in the cold room were analyzed for SF_6 and N_2O using the GC-ECD and the air-water concentration differentials at equilibrium (C_a) were determined in mol m^{-3} using

$$C_a = X * H \qquad (3)$$

Ice cores were taken daily to monitor ice thickness and the accumulation of SF_6 and N_2O in the ice through diffusion. Cores were melted in an airtight container with a pure N_2 atmosphere for later headspace analysis (Loose et al., 2011). Once the core was melted, it was shaken to expel all the gas from the water and a sample of gas was removed and analyzed with the GC-ECD. Concentrations were determined using the headspace method (Wanninkhof et al, 1987). Ice thickness and water depth were monitored using a Benthos PSA-916 sonar altimeter mounted on the bottom of the test basin looking toward the surface. A second core was taken each day for ice crystal structure analysis, which was done on-site at CRREL.

During the entire experiment a thermistor string collected temperature data at 1 cm (5 cm at the very top and bottom) intervals along a 65 cm depth range that extended from the air, through the ice and into the water. A handheld salinometer was also used daily to check the water column for stratification.

1.2.3. Data interpretation

The mass balance of an inert gas tracer was used to infer rates of flux from the water to the air and to the ice. Over short time intervals (i.e. days), the first order ODE of tracer conservation was used to determine these fluxes

$$\frac{dM}{dt} = F_{ice} + F_{air} \qquad (4)$$

$\frac{dM}{dt}$ is the change in tracer mass in the water through time, F_{ice} is the flux of tracer from the water to the ice and F_{air} is the flux of tracer from the water to the air. This equation states that there are no internal sources or sinks for the gas tracers and the only loss terms are the gas fluxes. F_{ice} was first determined using a numerical solution for gas diffusion so then

$$F_{air} = \frac{dM}{dt} - F_{ice} \qquad (5)$$

For the numerical solution, it is necessary to determine the bulk gas diffusion coefficient through the ice; this determination is described in the subsequent section.

1.2.3.1. Determining the diffusion coefficient, D

To estimate the flux of gas into the ice, values of the diffusion coefficient (D) were determined for SF_6 and N_2O using a finite difference solution to the one-dimensional diffusion equation through a porous medium

$$\frac{\partial C}{\partial t} = D\frac{\partial^2 C}{\partial z^2} \qquad (6)$$

Gas was assumed to move through the ice in the vertical direction (D=D_z). Horizontal diffusion (D_x) was not included, as the capillary structure of sea ice makes D_x much, much less than D_z (Golden, 2001).

Initial boundary conditions at the ice-water interface were set to the measured gas concentration in the water and the air-ice boundary was set to the measured air concentrations. The initial concentration of gas in the ice was zero for the long lead (91% ice cover), as the pool was gas-free when ice formed. A second model run was initiated for the short lead (96% ice cover) with the same boundary conditions except the initial gas concentration in the ice was set to the modeled profile concentration at the end of the long lead scenario.

Both models were run multiple times for each gas through a range of D values and the bulk concentration of gas in the ice through time was calculated for each D. The D chosen was that whose bulk concentrations had the smallest residual error between than and the measured bulk concentrations of N_2O and SF_6. Using Graham's Law ($\frac{D_a}{D_b} = \sqrt{\frac{m_b}{m_a}}$, where D_a and D_b are the velocities of two gases and m_a and m_b are their respective masses), the corresponding D for each of the other gases was calculated (Table **2**). The mean value of D from all four scenarios was used to estimate k_{ice} by dividing by a characteristic length scale of the diffusivity: the ice thickness $\left(k_{ice} = \frac{D}{z_{ice}}\right)$. Once D was determined, F_{ice} was calculated by

$$F_{ice} = A_{ice} * \frac{N*dz}{dt} \sum_{j=1}^{N} \left(C_j^{k+1} - C_j^k\right) \qquad (7)$$

A_{ice} is the surface area of the ice, N the number of nodes through the ice in the finite difference model, dz the thickness of a single node, and C the concentration of tracer in the ice at time k and node j.

1.2.3.2. Determining the gas transfer velocity, k_{eff}

The bulk concentration of each gas in the ice (C_{ice}) was determined using the finite difference model and subsequently the moles of gas (M) that were lost to the ice were "added back" to the measured gas in the test basin (C_w) to correct $\frac{dM}{dt}$ for this loss term:

$$\frac{dM}{dt}\Big)_{corrected} = \frac{dM}{dt}\Big)_{observed} + F_{ice} \qquad (8)$$

Additionally, the rate of change of tracer in the tank can be described as,

$$\frac{dM}{dt}\Big)_{corrected} = \frac{V_w dC_w(t)}{dt} \qquad (9)$$

Taking the integral of equation 8 with respect to time (t) results in

$$M(t) = V_w C_w(t) \qquad (10)$$

To solve for $C_w(t)$, we replace $F_{ice}(t)$ back into the water as

$$M_w(t) = M_{obs}(t) + F_{ice} * dt \qquad (11)$$

so that

$$C_w(t) = \frac{M_w(t)}{V_w} \qquad (12)$$

Finally, the corrected value of $C_w(t)$ can be used to calculate k_{eff} (Loose et al., 2014).

$$k_{eff} = \frac{h}{dt} \ln\left(\frac{C_{wi} - C_a}{C_{wf} - C_a}\right) \qquad (13)$$

h is the measured water depth in the pool, dt is the length of the scenario (days) and C_a is the concentration of gas in the air. A best fit line through the measured $C_w(t)$ for

each scenario (period of constant forcing conditions where the wind speed and water current did not change) was used to estimate the initial (C_{wi}) and final (C_{wf}) gas concentrations over the time period of an individual scenario.

Using the flux-gradient version of Fick's law ($F = -D\frac{dc}{dz}$) near the top of the ice we estimated the gas transport at the air-ice interface and found it to be null. In other words, gas appeared to diffuse into the ice, but diffusive transport from the water to the air (through 20 cm of ice) was negligible over a period of ca. 30 days (Figure **6**). All values of k_{eff} were normalized to a k_{600} using the Schmidt number relationship $k_{eff} = k_i\left(\frac{600}{Sc_i}\right)^{-0.5}$. We used formal error propagation following the method described in Glover et al. (2011) to determine the level of precision of each individual estimate of k_{eff} (Appendix A). The individual k_{eff} values for each tracer gas during each scenario were also averaged and the empirical error was calculated as the standard error between these. These two errors were compared to determine the constraint achieved on the mean value of k_{eff} calculated for each scenario (Table 3).

1.2.3.3. Determining velocity and u_*

The hourly averaged velocity profiles were again averaged over each scenario and the water velocity was set as the mean velocity of the averaged profile (Figure **7**). The profiler was configured to sample up to the air-water or water-ice interface. Velocity profiles of each scenario were plotted against the log of depth below this interface. The log-linear portion of the velocity profile was used to determine u_* (friction velocity) and z_0 (roughness height), in a least-squares sense, using

$$U(z) = \frac{u_*}{\kappa} log_e\left(\frac{z}{z_0}\right) \qquad (14)$$

where $U(z)$ is the velocity as a function of height off the bottom (z), and κ is the von Karman constant, which has a universal value of 0.41. k_{eff} for each scenario was plotted against both the average water velocity and u_* for each scenario to determine if either value can explain the forcing event in a comparable manner.

1.3. Results

The concentration of SF_6, N_2O and ^3He decreased monotonically over time in the test basin reflecting gas evasion. In Figure **4**, it is evident that the rate of decrease varied depending on the forcing conditions present in the basin. When analyzing the helium samples, we observed concentrations in excess of saturation for ^4He and Ne. ^4He had a much greater supersaturation than Ne, and the concentration of ^4He decreased, while that of Ne increased during the experiment (Figure **5**). Analysis of the carbonate system in the test basin determined that the water in it had an alkalinity of approximately 3.8-3.9 mM and an anomalous DIC compared to that of normal ocean water.

Salinity values in the test basin through the experiment are shown in Figure 3. Increases of up to 1 ppt occur during ice formation (day 0 to 3, day 16 to 21) when large amounts of brine are rejected from the ice during freezing. By dividing the increase in salinity by the change in ice thickness it was determined that an approximately 0.1 ppt increase resulted from every centimeter of ice grown. Smaller variations of hundredths to tens of a ppt were evident during some scenarios. These small increases result from a small amount of frazil ice formation on the water surface or air temperature raising causing the ice to warm and the brine to drain out of it (Petrich and Eicken, 2009). Small decreases may result from erosion of the underside

of the ice and subsequent melt (day 22 to 25, day 27.5 to 29.5). Yet through most scenarios salinity remained fairly constant.

Vertical profiles of conductivity-temperature-depth were carried out to observe stratification present in the tank. The profiles, converted to density shown in Figure **8**, show a uniform, stable water column indicating water in the test basin was well mixed through the experiment. There are a few instances (dotted lines) when the water column appears denser at the surface. This is likely an artifact resulting from salt crystals on the salinometer as well as its limited precision.

Figure **9** shows microscopy of the ice crystal structure that was carried out at CRREL. Vertical and horizontal thin sections under cross-polarization indicate that the ice formed in the test basin had a very similar structure to that occurring in natural sea ice. Brine channels are clearly identifiable in these images; crystals near the ice-air surface are much smaller than those near the water-ice boundary due to the initial formation of frazil that is disaggregated before the columnar dendritic structure takes over (Petrich and Eicken, 2009).

The thermistor string frozen into the ice revealed a temperature gradient through the ice ranging from -9°C at the cold air-ice interface to -1.5°C at the ice-water interface. This is evident in Figure 10. The gradient was greatest when a large air-water temperature differential was present. As expected, the ice is coldest at the surface and warms towards the ice-water interface. This is very clear during the short lead scenarios (day 22 to 30). Here, the air temperature is not as cold as the goal is to avoid freezing or melting of the ice, so the gradient is less but still present ranging from about -5°C at the ice-air interface to -1.5°C at the ice-water interface.

We increased the room temperature at times to discourage frazil ice formation over the lead during scenarios with wind. This resulted in the surface temperature of the ice increasing and, when air temperature warmed (above the freezing temperature on day 26 to 27), an inverted gradient is evident though the ice; the very surface is warm (-0.8°C) and then gets colder (-1.8°C) about 3 centimeters in where the heat from the room has not yet penetrated before warming to -1.5°C as the temperature of the deep ice equilibrates with the water in the test basin.

Figure **11** shows the bulk measured and modeled concentrations of SF_6 and N_2O in the ice determined from the finite difference model run with the magnitude of D ranging from 10^{-5} to 10^{-7} cm^2 s^{-1}. From this, it is evident that the best fit of the measured data is when D is around 10^{-6} cm^2 s^{-1}. This results in a bulk ice concentration of approximately $2x10^{-3}$ mol m^{-3} N_2O, $4x10^{-8}$ mol m^{-3} SF_6 and $7x10^{-10}$ mol m^{-3} ^3He. F_{ice} accounted for less than 2% of the total amount of tracer lost from the test basin through the experiment.

The range of the k_{eff} values found during each scenario is displayed in Figure **12**. It is evident that increases in the gas transfer velocity occur when all conditions remain constant and pump speed increases from 20 to 60 Hz (scenario 1 vs. 2), wind speed increases from 20 to 60 Hz (scenario 3 vs. 4) and the amount of open water increases from 4% to 9% (scenario 1 vs. 5 and scenario 3 vs. 6). It is also evident in Figure **12** that the individual tracer gases (SF_6, ^3He, N_2O) do not always give the same value of k_{eff}. This is especially true for scenario 7 where the forcing from both the pumps and the wind was high.

Estimates of the gas measurement error in both the ice and water concentration were propagated through equations 4 to 13, which are used to calculate individual values of k_{eff} for each gas. We observed that this formal calculation of error was consistently smaller than the standard error of k_{eff} estimated from SF_6, N_2O and ^3He (Table 3). Ideally, the Schmidt number model should account for any gas dependency in the estimate of k_{eff} for each tracer gas, yielding estimates of k_{eff} during a given scenario that are identical. The existence of a standard error between the gases, which exceeds the magnitude of the standard error from the propagation (Appendix A), indicates that other sources of variability in the measurements exist which have not been accounted for. One example of such a process is the release of brine from the ice and localized erosion of the ice from the water circulating beneath. Both processes can affect the gas budget (Loose et al., 2009), but are difficult to quantify. Given that the standard error between gases exceeded the formal error propagation, we opted to use the standard error to establish the level of significance of our estimates of k_{eff} during each of the scenarios with unique gas exchange forcing conditions. The error bars in Figure 12 and Figure 13 reflect this significance level.

Profiles of the water velocity in the wind tunnel during high pump (a) and high wind (b) conditions are shown in Figure **7**. It is evident that the water velocity is much more influenced by the pump speed than the wind speed, as water velocity reached 0.156 m s^{-1} when the pumps were high yet fell to 0.015 m s^{-1} when the pumps were low and wind was high (Table **1**). Values of u_* represent the shear present at the surface which is much greater during wind events. Thus, u_* values were greater during high wind events than low wind events (0.0263 m s^{-1} vs. 0.0038 m s^{-1} respectively).

1.4. Discussion

1.4.1. Carbonate system in the test basin

The carbonate chemistry of the test basin was analyzed to help us in our interpretation of the pCO_2 data. As the tank had a very large oversaturation of CO_2, it was hoped that the addition of 98% NaCl as salt to fresh water would result in an alkalinity in the tank of 0 eq m^{-3} allowing any change in DIC to be due to changes in pCO_2. Unfortunately, the water in the test basin was found to have very high alkalinity (3.8-3.9 mM) and low DIC compared to normal ocean water (DIC ~ 2mol C m^{-3}, Alkalinity ~ 2.2 eq m^{-3}) (Pilson, 2013). Analysis of a sample of the salt added to the pool found that it has approximately 1mM DIC and 2 mM alkalinity. Further calculation determined the 2% of the salt that was not pure NaCl could have been pure phosphate (5.7mM in the test basin), hydroxide (32mM in the test basin), bicarbonate (8.9mM in the test basin) or, more likely, a combination of these and other alkaline compounds. Our inability to constrain the carbonate system in the test basin resulted in our not attempting to analyze the time series of pCO_2 and observe how it compared with the other gas budget calculations.

1.4.2. Gas flux

1.4.2.1. Neon and helium

Figure **5** shows the concentrations of ^{4}He and Ne over time in the test basin. ^{4}He and Ne were not purposefully introduced to trace gas fluxes. However, it is likely that they became supersaturated while bubbling air into the tank to aid in mechanically agitating and dissolving the NaCl crystals before the beginning of the experiment. At the beginning of the experiment the concentration of ^{4}He is much more supersaturated

than Ne. ^{4}He's saturation (and concentration) then decreases through the experiment similar to ^{3}He, N_2O and SF_6. Ne was only slightly supersaturated at the beginning and its concentration increases during the period of 91% ice cover and then decreases slight or remains flat for the remainder of the experiment (96% ice cover). This unique behavior of both Ne and ^{4}He is likely due to their presence in the tank before freezing and, thus, their incorporation into the ice. Therefore, while the behavior of the other gases was governed by the high concentration differential between the water and air (with no tracer present in the ice), the change in Ne concentration resembles that of a gas leaving the ice via brine rejection and during freezing. ^{4}He resembles a gas that is both rejected from the ice and escaping through the air-water interface.

Using the equations of Cox and Weeks (1983), we calculated that about 2.75 m^3 of brine with a salinity of 55 ppt drained from the ice. Provided Ne, ^{4}He and salt are incorporated into the brine equivalently (Loose et al., 2009), brine drainage can account for approximately half of the increase seen in the Ne concentration. After accounting for brine drainage the value of k_{eff} from ^{4}He is consistent with the k_{eff} of ^{3}He.

The remainder of the increase in Ne concentration is likely the result of freezing. During the freezing event for the short lead there is a 1% increase in the concentration of Ne in the water. During this same period, approximately 5% of the liquid volume in the tank is frozen. Studies have shown that during ice formation 90% of the neon is incorporated into the ice matrix while 10% is rejected into the water (Top et al., 1988). Thus, if there is ~5% oversaturation of neon in the tank, the increase in its concentration during ice formation can be explained by solute rejection.

Freezing likely occurs over days 8 to 11 (Figure **5**), a time of high winds and low pumps so frazil ice formation is an issue. The observed decrease in Ne after day 20 is likely due to gas exchange and ice melt, as the air temperature was warm during this period and the salinity in the tank decreased (Figure 3).

The difference in the behavior of Ne and ^{4}He is likely a result of the difference in their levels of supersaturation and size. As ^{4}He has a larger concentration gradient between the air and water than Ne, it has a greater tendency to evade the water. Also, Ne is five times heavier than ^{4}He and so is going to move through the air-water interface at a slower rate. Thus, Ne's concentration is mostly impacted by rejection from the ice while ^{4}He's is influenced more by gas exchange.

^{3}He, N_2O and SF_6 are not as influenced by these processes due to their absence from the ice as well as their large concentration gradient between the air and water.

1.4.2.2. Diffusion coefficient, D

Figure **11** shows that the diffusion coefficient best fits the data when on the order of 10^{-6} cm^2s^{-1}. Interestingly, using the raw, modeled data, SF_6 was found to have a faster diffusion rate than N_2O. This does not follow Graham's Law as SF_6 is a larger, heavier molecule than N_2O, and once the conversions were done, this was no longer the case. Interestingly, Loose et al. (2011) found a similar trend between the diffusion coefficients of SF_6 and O_2 and suggested the trend could be due to differences in solubility between the gases.

Diffusion coefficient values around 10^{-6} cm^2s^{-1} are about an order of magnitude lower than the diffusion of gas through water which are on the range of 10^{-5} cm^2s^{-1} (Himmelblau, 1964; Jähne et al., 1987) and a factor of ten larger than the diffusion of

gas measured in glacial ice which is on the order of 10^{-7} cm^2 s^{-1} (Ahn et al., 2008). The set crystal structure of the ice likely slows the rate of diffusion as liquid water freezes into solid ice. Figure **6** shows the concentration gradient of N_2O across the ice at the end of the final lead experiment. From this, it can be seen that only a very small amount of tracer is incorporated into the ice and none diffuses fully across the ice and into the air. Thus, neither *D* nor the gas flux through the ice to the air is of great consequence to air-sea gas transport.

^{3}He diffusion values were determined through application of Graham's Law to the SF_6 and N_2O values. This diffusion coefficient unfortunately does not account for any preferential incorporation of ^{3}He into the ice crystal lattice due to its very small size (Namiot and Bukhgalter, 1965). But, Figure **12** shows that the k_{eff} values of ^{3}He are in line with those of N_2O and SF_6, so any preferential incorporation of ^{3}He into the ice is likely not influencing k_{eff} greatly.

1.4.2.3. Gas transfer velocity, k_{eff}

We observed an increase in k_{eff} when the water current and/or wind forcing was increased, as well as when ice cover was reduced (Figure **12**, Table **1**). Research in the past has shown that k_{eff} increases with wind speed and the amount of open water, but here it is clear that the water velocity plays an important role in ice-covered areas as well. This is likely a result of turbulence at the ice-water interface and will therefore be important in areas with high water currents flowing under a large volume of ice.

One exception to this trend occurred during high wind (60 Hz), low water current (5 Hz) and very low fraction of open water (f = 0.04) conditions (scenario 6).

At this time, it appears the area of open water was too small for much turbulence to develop even though there was a strong shear at the surface (Figure **7**) and, as a result, gas exchange was small. Salinity changes during this period were also small so it is unlikely that ice formation or melt was affecting the system at this time. The transfer velocity when the pumps were added (increased from 5 to 40 Hz, scenario 7) to this scenario increased by a factor close to seven indicating the importance of turbulence created by the pumps (Figure **12**, Table **1**). A similar effect was seen via increasing the fraction of open water from 0.04 to 0.09 (scenario 1 to 5 and scenario 3 to 6).

Unfortunately, the standard error between the k_{eff} of the three tracer gases during scenarios with small fractions of open water (f = 0.09 and 0.04), were larger than we would have liked and consistently greater than the error propagated through the equations (Table 3, Appendix A). Thus, the error of the calculation does not account for all of the variance that is seen between the three tracer gases. This could be a result of ice formation and melt during the scenarios and ice having different affinities for the different tracer gases. Frazil ice formation complicates air-sea exchange by several mechanisms and was a recurring process during scenarios 4 and 6 (Table 1), as the water current was low at these times and the wind blew cold air across the water surface causing it to quickly freeze. Melt was an issue during scenarios 5 and 7 as the air temperature was increased to reduce the formation of frazil. These processes likely resulted in some of the variability that we observed during these periods. Each of these processes can account for only a very small (<5%) change in k_{eff}, so the inconsistency seen in the k_{eff} is due to many different variables.

Another factor that may have resulted in some error is the circulation pattern of the test basin at CRREL. At one end of the test basin there are multiple pipes that connect to a 61.6 m^3 fully enclosed tank. No water was pumped between the tanks, but a pressure gradient resulting from the pressure of the water current pumps as well as diffusion likely resulted in some exchange and dilution of the tracers in the test basin. A pressure differential would only form during a major change in the water current of the main tank and would quickly equilibrate. Therefore, this likely did not result in a great deal of transfer between the tanks. But, N_2O and SF_6 were in the tank for a month before ^3He was added allowing their concentrations more time to equilibrate between the test basin and the additional tank. Thus, their concentrations are likely higher in the enclosed tank and the ^3He data would be more affected by dilution from this tank than the other two gases.

Figure **13** and Figure **14** show that neither the mean water velocity nor u_* can be used to explain all the trends seen in k_{eff}. The mean velocity of the water column does not account for the shear caused by the wind and therefore underestimates k_{eff} in high wind conditions. The value of u_*, meanwhile is only a measure of the shear at the air-water boundary and is thus not affected by the pumps as they increase the velocity of the entire water column. Thus, u_* underestimates k_{eff} in high current conditions and the mean water velocity underestimates k_{eff} in high wind conditions. Another measure is therefore needed to better constrain the forcing and relate to k_{eff}, and this is a work in progress.

Figure **13**b shows mean water velocity vs. k. The conversion from k_{eff} to k removes the influence of the fraction of open water allowing a representation of just

the forcing (wind and water current). By far the largest k occurs at a water velocity of 0.12 m s^{-1} and wind speed of 5.25 m s^{-1} when both the pumps (40 Hz) and fan (60 Hz) are on. Of the three k values of approximately 3 m day^{-1}, two occur when the pumps are at 60 Hz (water current of ~0.15 m s^{-1}) and the wind is off. Just the turbulence of the water motion is resulting in a large amount of gas exchange in both these scenarios. The third scenario with a k of approximately 3 m day^{-1} is wind driven, as the fan is at 60 Hz and the pumps are very low. This is further evidence that, in the seasonal ice zone, it is important to consider both the wind speed and water currents under the ice when determining gas exchange rates.

In summary, the GAPS Experiment performed at CRREL found that, in the presence of sea ice, the magnitude of k_{eff} is influenced by the fraction of open water, wind speed and water current speed. An escalation of each of these factors results in a significant increase in the rate of gas exchange. This is shown in Figure **12**. Unfortunately, neither the mean water velocity nor u_* can be directly related to the magnitude of k_{eff} as mean water velocity accounts for the turbulence and gas exchange resulting from the pumps while u_* accounts for the shear and gas exchange caused by the wind. Therefore, a different measure of the turbulence that can account for both of these factors is needed to explain the effects of both types of forcing at once. It was also found that the D is on the order of 10^{-6} cm^2 s^{-1} and is small enough so that the flux of tracer into the ice is insignificant to the value of k_{eff}.

TABLES

Table 1. Forcing scenarios conducted during the GAPS experiment at CRREL and the results of each.

Scenario Number	Fraction of Open Water	Pump Speed (Hz)	Fan Speed (Hz)	Water Velocity (m s^{-1})	Wind Speed (m s^{-1})	u_* (m s^{-1})	Mean k_{eff} (m day^{-1})
1	0.09	60	0	0.145	0	6.00E-4	0.245
2	0.09	20	0	0.045	0	---	0.140
3	0.09	5	60	0.015	5.25	0.0263	0.301
4	0.09	5	20	0.017	1.85	0.0214	0.0296
5	0.04	60	0	0.156	0	0.0044	0.127
6	0.04	5	60	0.0253	5.25	0.0231	0.0432
7	0.04	40	60	0.120	5.25	0.0038	0.300

Table 2. Diffusion coefficients, *D*, of the gases moving through the ice. N_2O and SF_6 values were determined using a finite difference model fit to measured bulk gas concentrations in the ice. Values in italics are those determined from the model and subsequent values were determined using Grahams Law. All values of D are $cm^2\ s^{-1}$.

Scenario	**D_{N2O}**	**D_{SF6}**	**D_{He}**	**D_{Ne}**
0.09 Open Water	*$2.9x10^{-6}$*	$1.6\ x10^{-6}$	$9.8\ x10^{-6}$	$4.3\ x10^{-6}$
0.09 Open Water	$8.2\ x10^{-6}$	*$4.5\ x10^{-6}$*	$2.7\ x10^{-5}$	$1.2\ x10^{-5}$
0.04 Open Water	*$2.4\ x10^{-6}$*	$1.3\ x10^{-6}$	$8.0\ x10^{-6}$	$3.6\ x10^{-6}$
0.04 Open Water	$1.2\ x10^{-5}$	*$6.5\ x10^{-6}$*	$3.9\ x10^{-5}$	$1.8\ x10^{-5}$
Average	**$6.4\ x10^{-6}$**	**$3.5\ x10^{-6}$**	**$2.1\ x10^{-5}$**	**$9.5\ x10^{-6}$**
Standard Deviation	$4.6\ x10^{-6}$	$2.5\ x10^{-6}$	$1.5\ x10^{-5}$	$6.8\ x10^{-6}$

Table 3. Percent error of the k_{eff} values for each tracer gas during each scenario calculated using the rules of error propagation and found empirically as the standard error between the k_{eff} calculated for each tracer during each scenario.

Scenario	% Error Propagated for N_2O	% Error Propagated for SF_6	% Error Propagated for ^3He	% Error Empirical
1	7.07	7.01	---	10.5
2	3.45	11.5	1.23	21.3
3	1.97	5.82	0.830	2.54
4	10.7	54.7	3.09	235
5	3.08	2.06	3.36	54.2
6	6.97	3.44	1.54	168
7	4.41	3.80	---	75.4

FIGURES

a.

b.

c.

Figure 1. The test basin at CRREL. a). View looking west across the test basin. The wind tunnel is along the left hand side and the box containing the fan is shown. b). View looking east across the test basin. The end of the wind tunnel is seen on the right. c). Velocity profilers in the wind tunnel with the water circulating pumps in the background

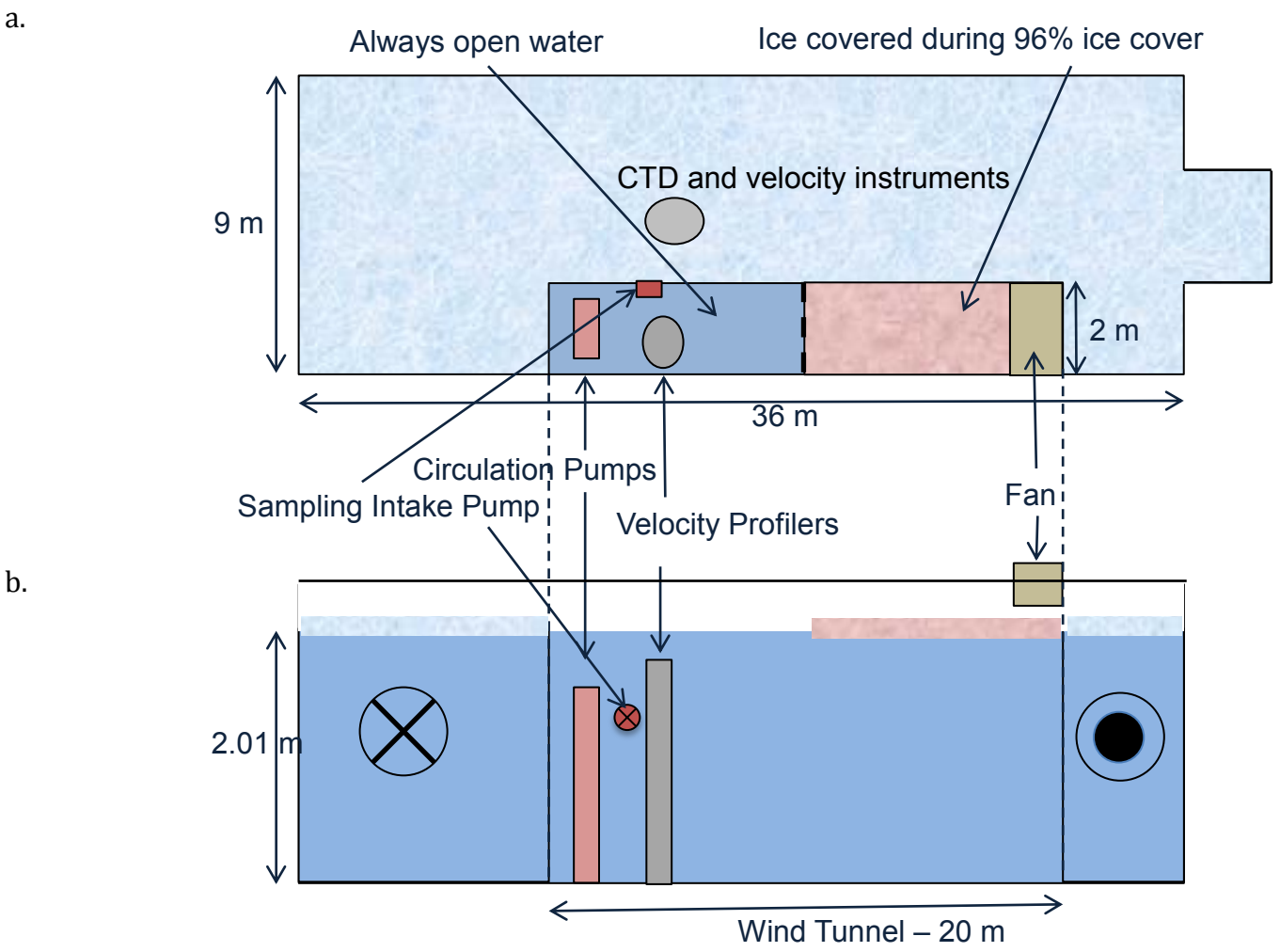

Figure 2. Diagram of the CRREL Test Basin set-up for the GAPS Experiment. a). Plan view. b). Section view. Entire wind tunnel was ice free during 91% ice cover experiments. Pink indicates ice cover during 96% ice cover experiments.

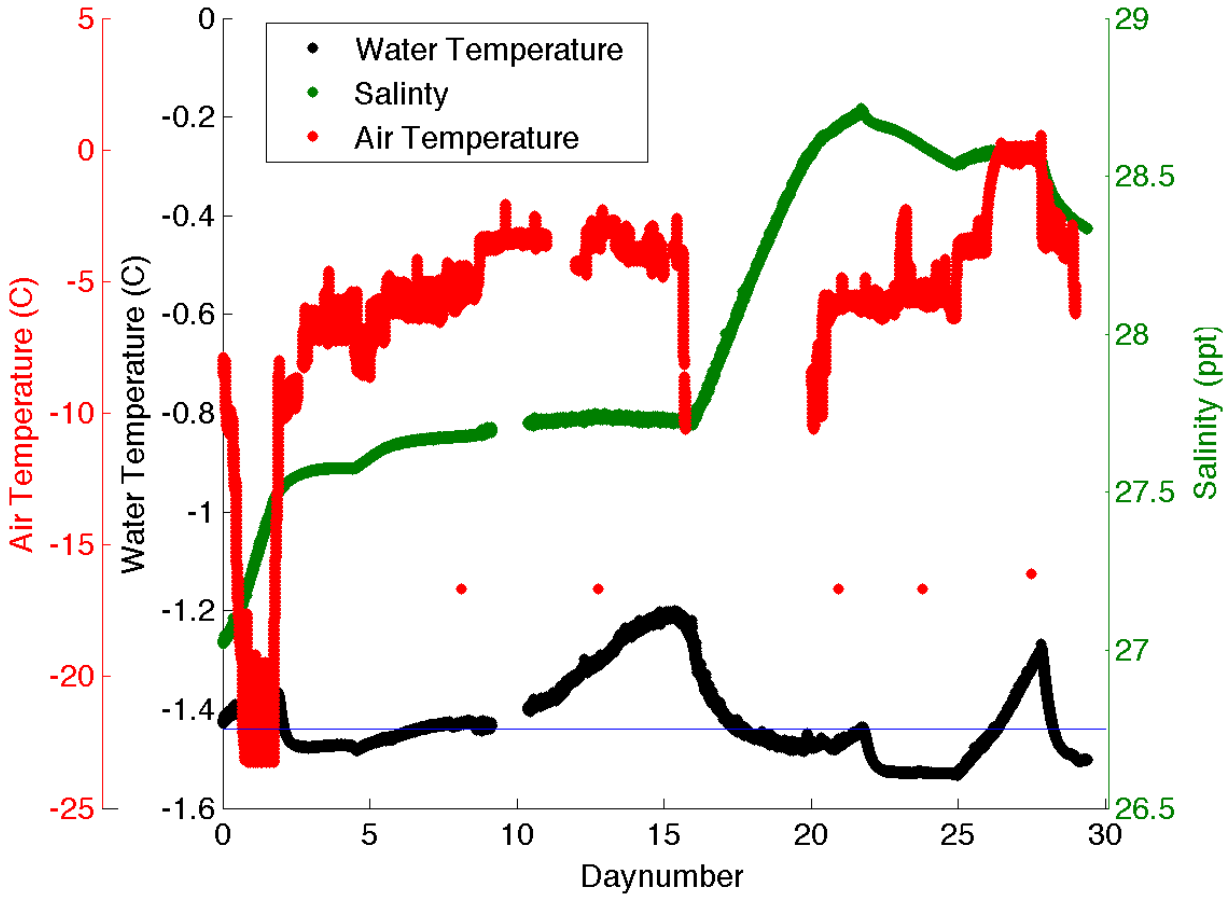

Figure 3. Air and water temperature as well as salinity of the test basin throughout the GAPS experiment. The blue line indicates the freezing point at approximately 28 psu.

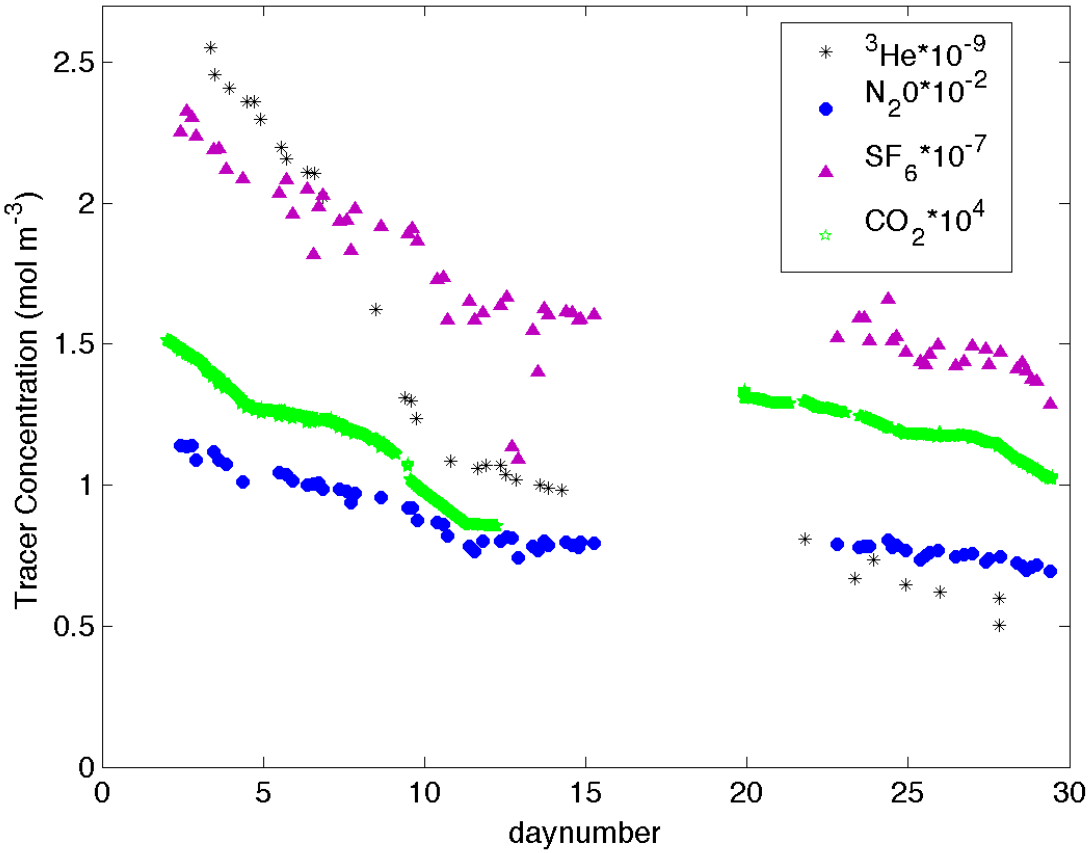

Figure 4. Concentration of the four tracer gases (^{3}He, N_2O, SF_6 and CO_2) whose concentrations were intentionally spiked in the test basin decreasing with time. The rate of decrease varies depending on the conditions present in the test basin. CO_2 data was not used due to uncertainties regarding the carbonate system in the test basin.

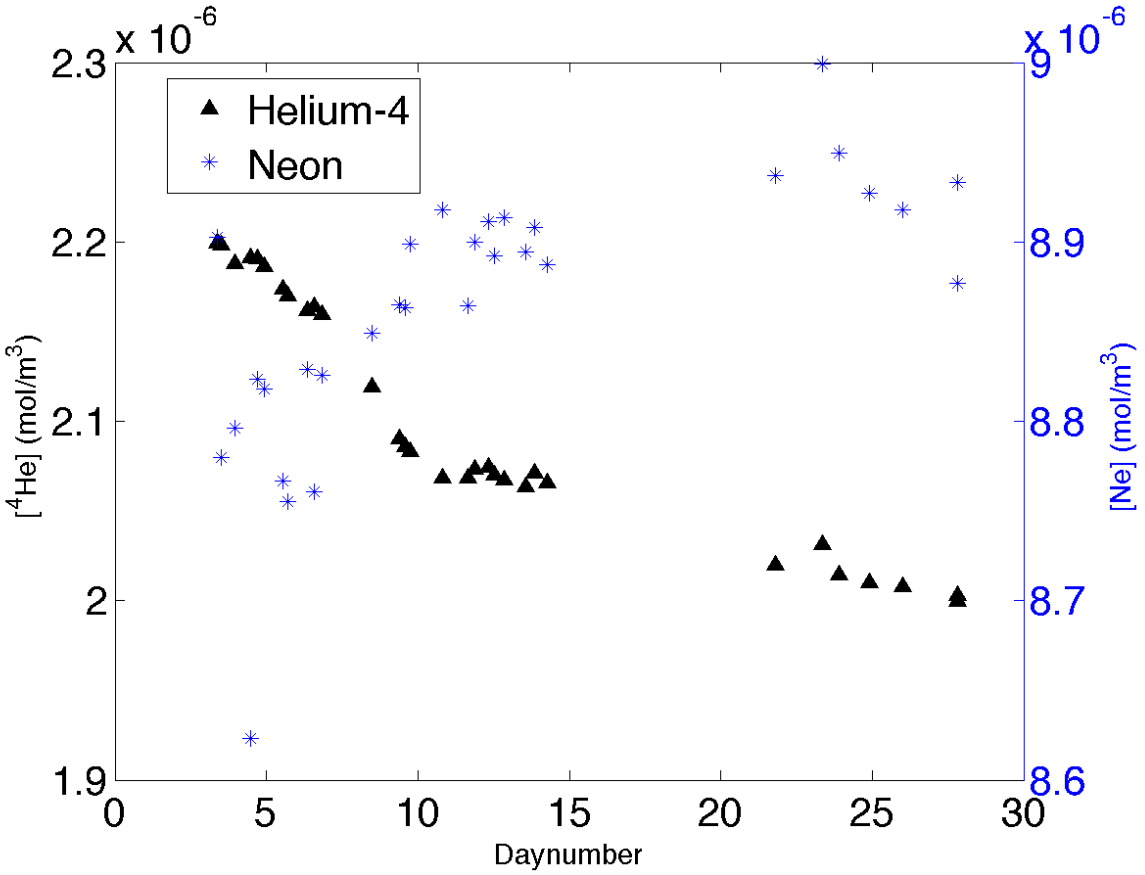

Figure 5. Concentration of ^{4}He and Ne in the test basin during the experiment. Both these gases entered the tank as a result of bubbling the water with air when dissolving the salt. Ne's concentration increases as it is barely supersaturated and is rejected from the ice during freezing. ^{4}He is also rejected from the ice but its concentration decreases as it is also escaping through the air-water interface at a rate much fast than Ne due to its greater supersaturation and smaller size.

a.

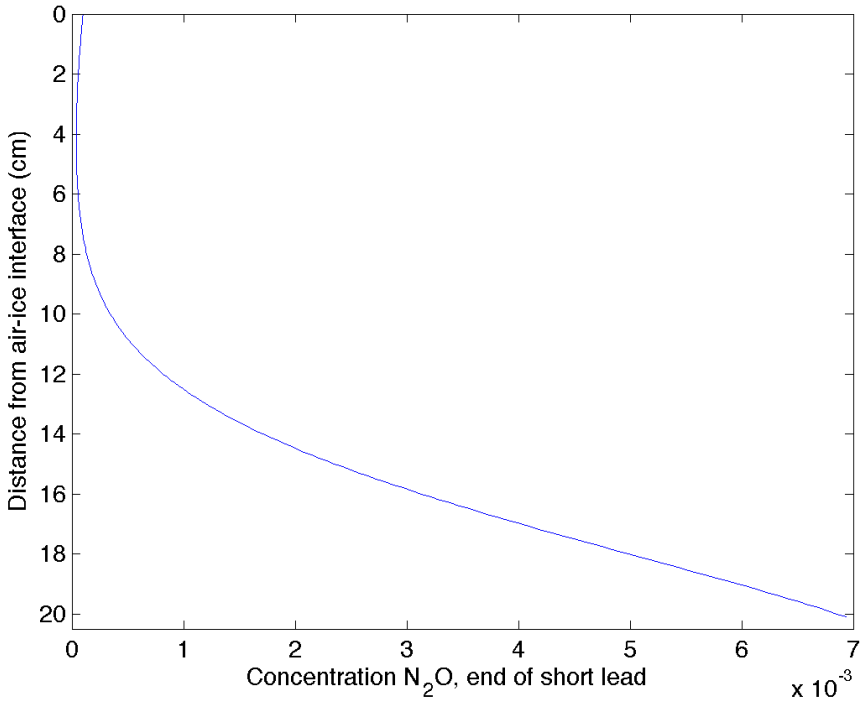

b.

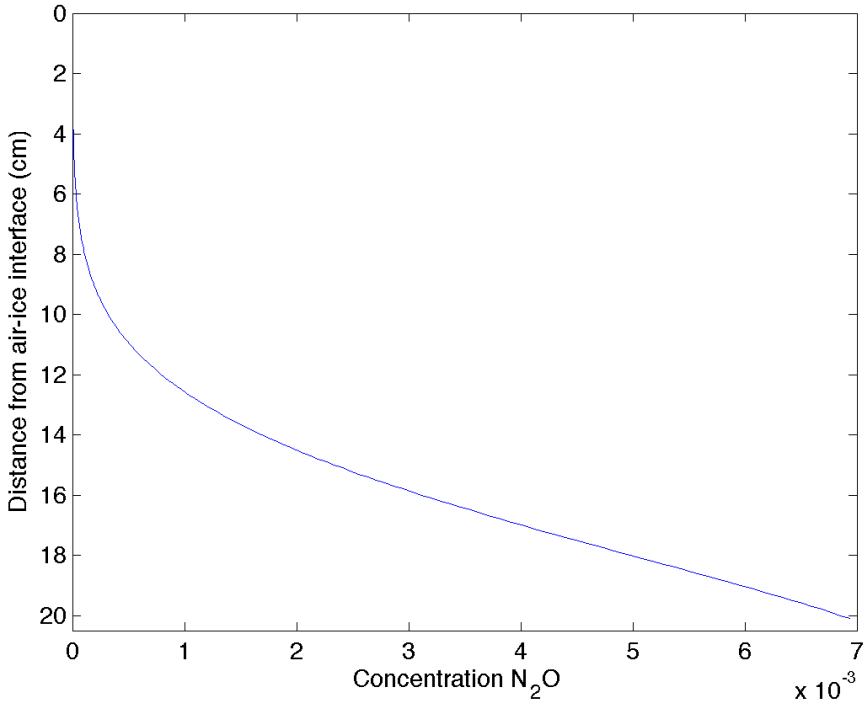

Figure 6. Concentration profile of N_2O across the ice at the end of the experiment. a). accounting for the air concentration of N_2O b). if there is no N_2O present in the air.

a.

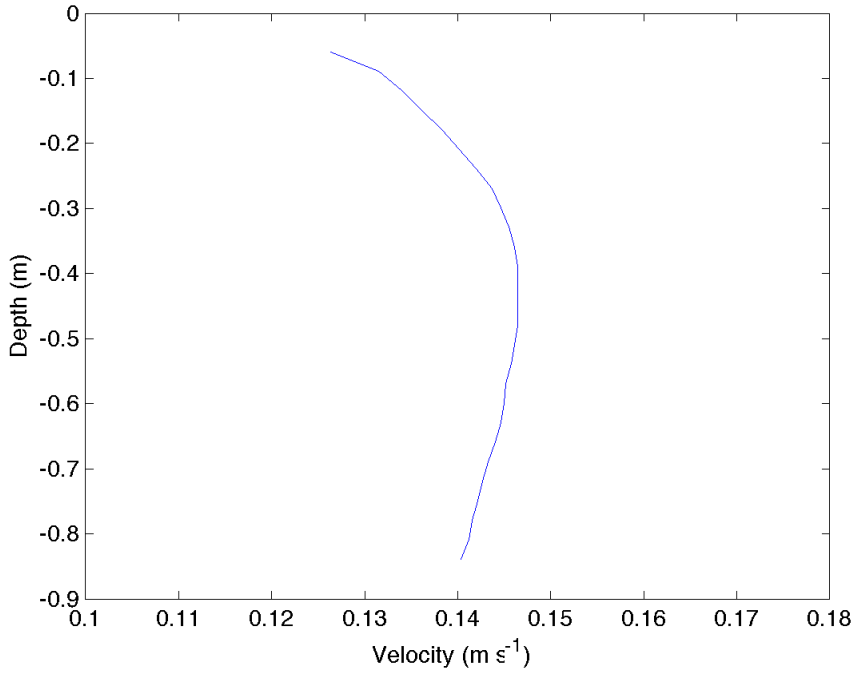

b.

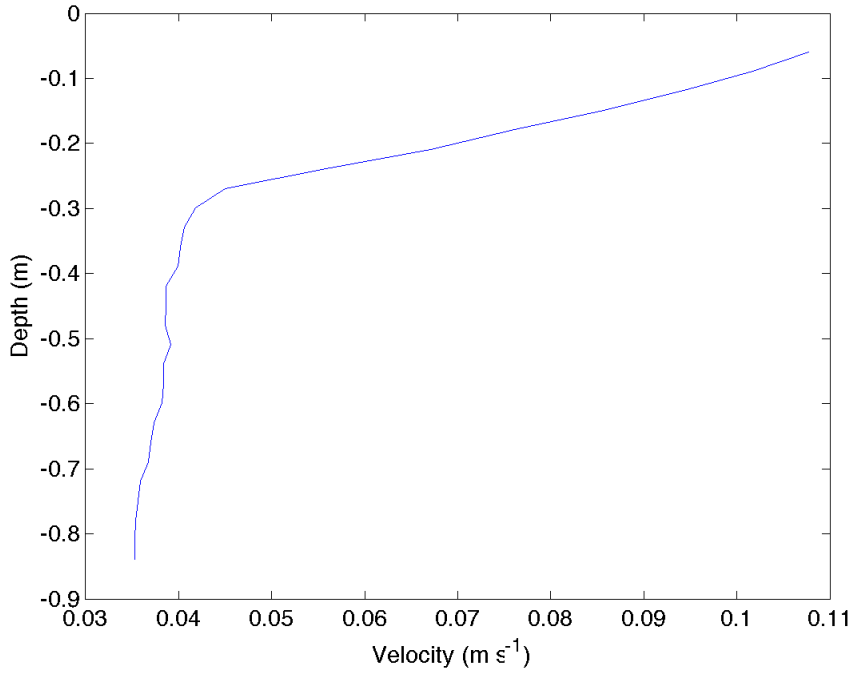

Figure 7. Averaged profile of the water velocity in the wind tunnel during a). high pump (scenario 5) and b). high wind (scenario 6) conditions. The shear at the surface is much greater during high wind, as well as focused in the opposite direction from when the pumps are on high.

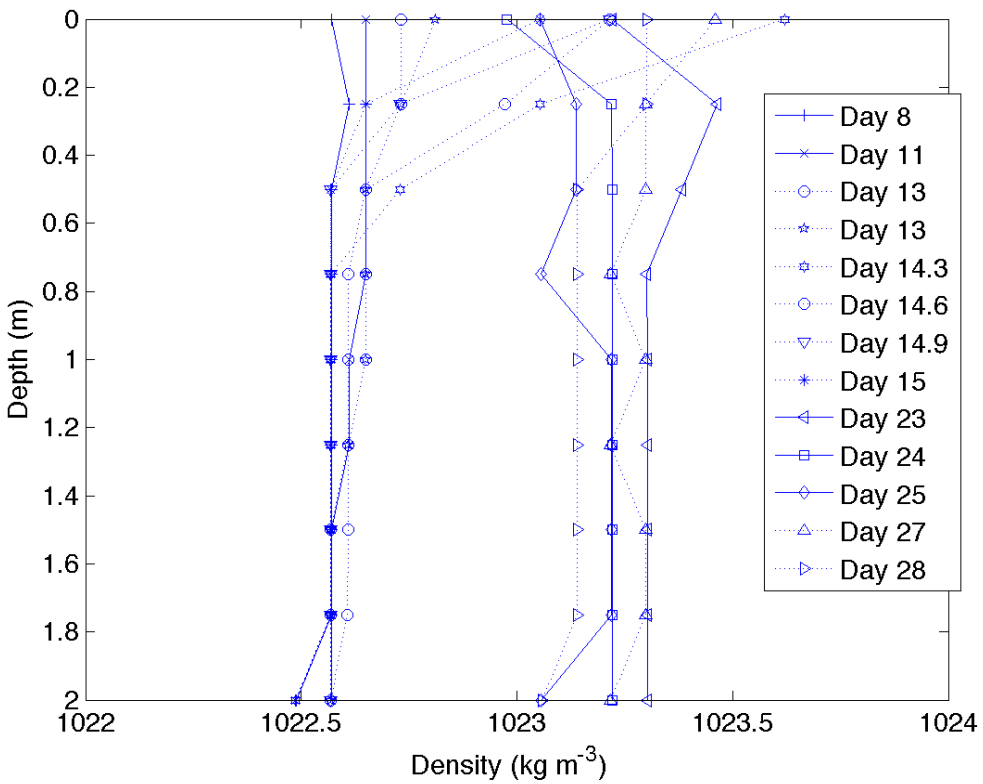

Figure 8. Density profiles calculated from temperature and salinity measurements taken at the western end of the wind tunnel in the test basin. Solid lines represent times of constant conditions and a stable water column. Dotted density profiles represent times of higher density measurements at the water surface. This density inversion is possibly an artifact of salt crystals on the conductivity cell of the hand-held salinometer used to make these readings. Overall, these profiles convey the test basin was well mixed.

a.

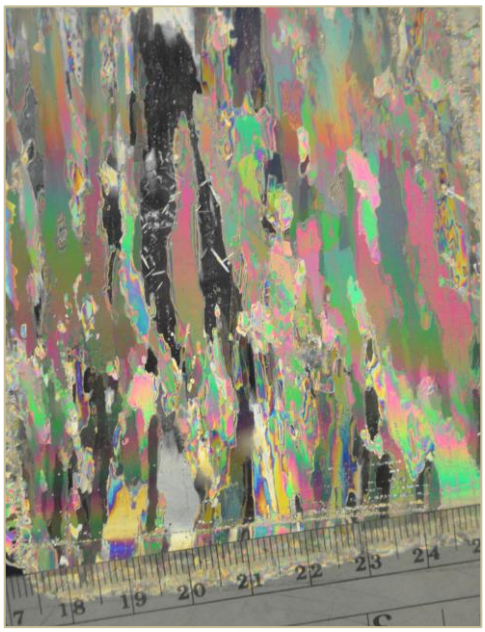

b.

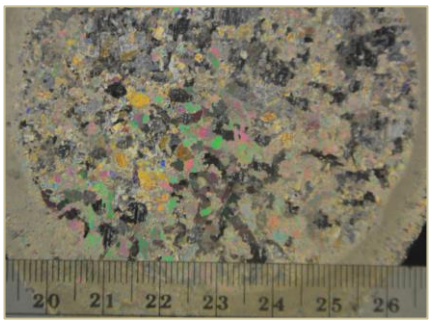

c.

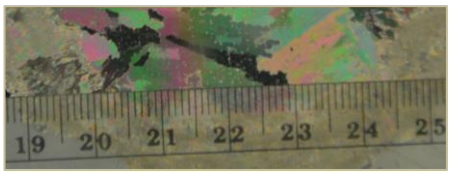

Figure 9. Cross-polarized thin section micrography of the laboratory sea ice grown in the test basin at CRREL during the GAPS Experiment. Individual ice platelets of differing geometries can be seen separated by brine channels oriented in the vertical direction. a). Vertical cross section. b). Horizontal cross section taken at the top of the core showing small crystals near the warm ice-air interface. c). Horizontal cross section taken at the bottom of the core showing the much larger crystals near the ice-water interface.

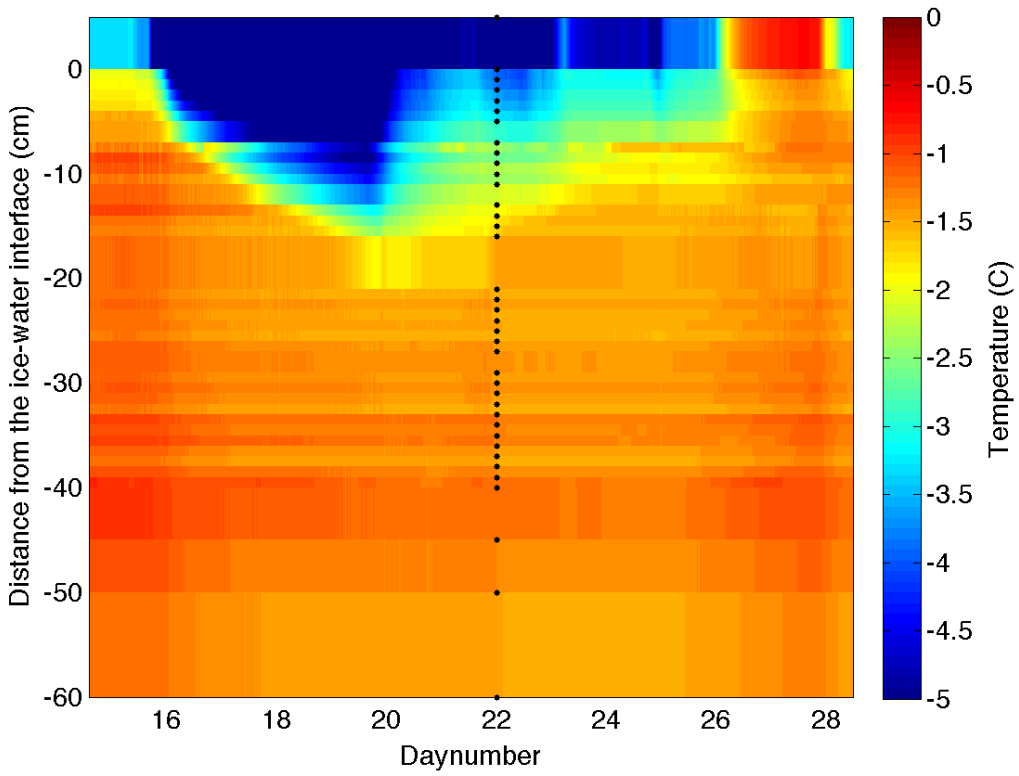

Figure 10. Temperatures observed in the thermistor string ranging from the air, through the ice into the water from Day 15 to 29. A much stronger temperature gradient and colder ice temperatures are evident at colder air temperatures. Zero depth marks the ice-air interface and black dots indicate the depths of the thermistor sensors where temperature measurements were taken every 5 minutes.

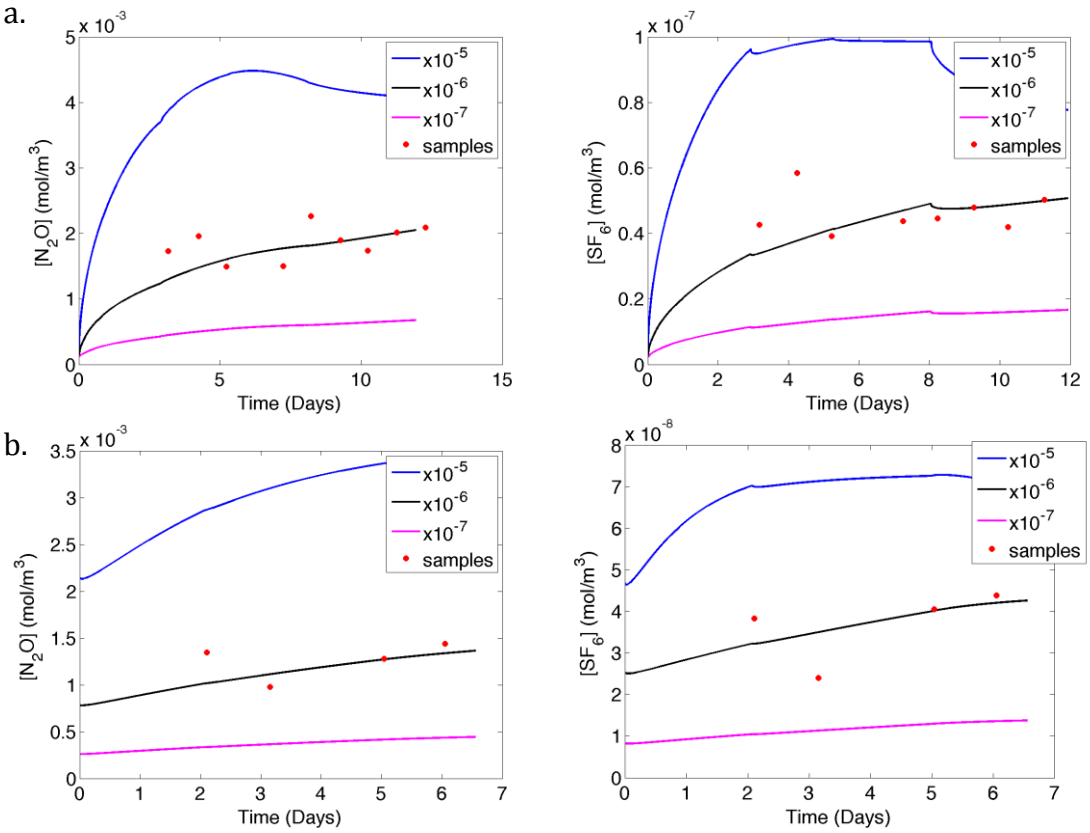

Figure 11. Model results for the diffusion coefficient (D) of N_2O and SF_6 into the ice for both the a). long and b). short lead. Red dots show the measured bulk concentration of the tracer in the ice. The smallest residual of error between the measured and modeled concentrations for both N_2O and SF_6 resulted from D values on the order of 10^{-6} cm^2 s^{-1} (black line). Inflections in the concentration are a result of changes in the ice-water boundary condition as tracer concentration in the water changed between scenarios.

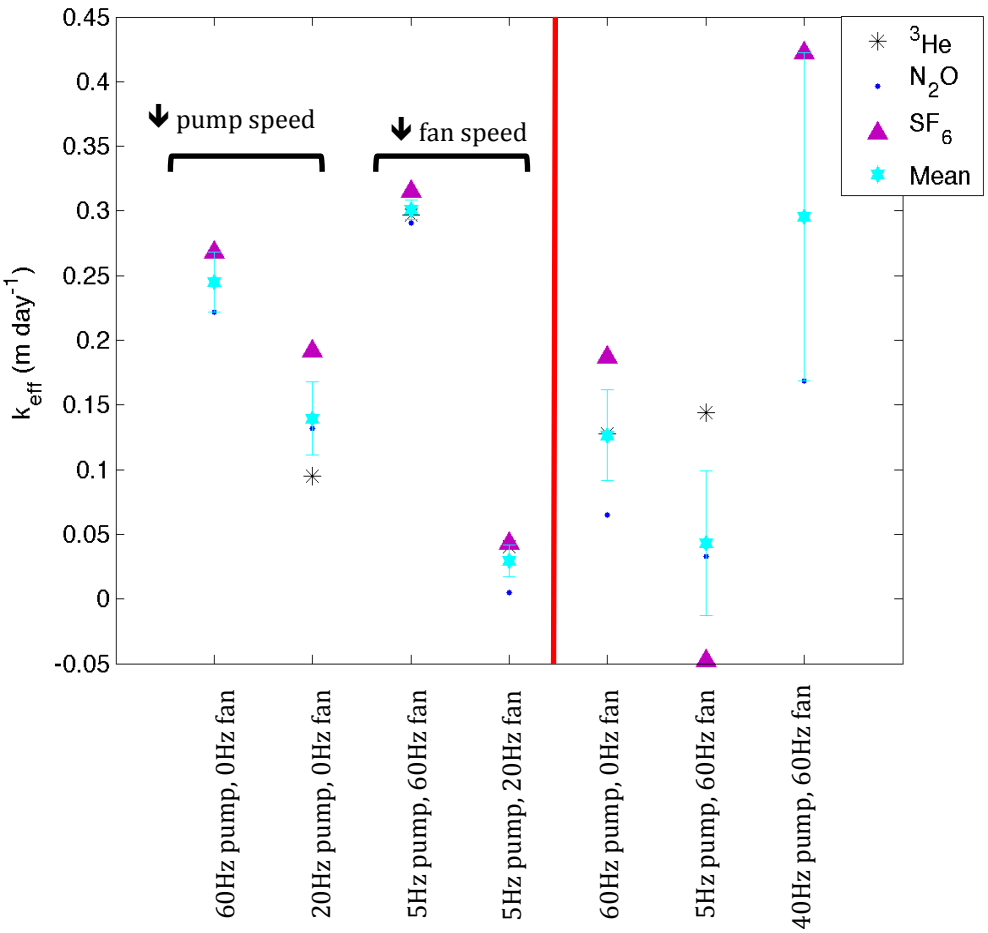

Figure 12. k_{eff} values for each forcing event, in order of scenario number. Error bars are the standard error of k_{eff} between the gases for each scenario. The red line separates 9% ice cover (to the left) from 4% ice cover (to the right).

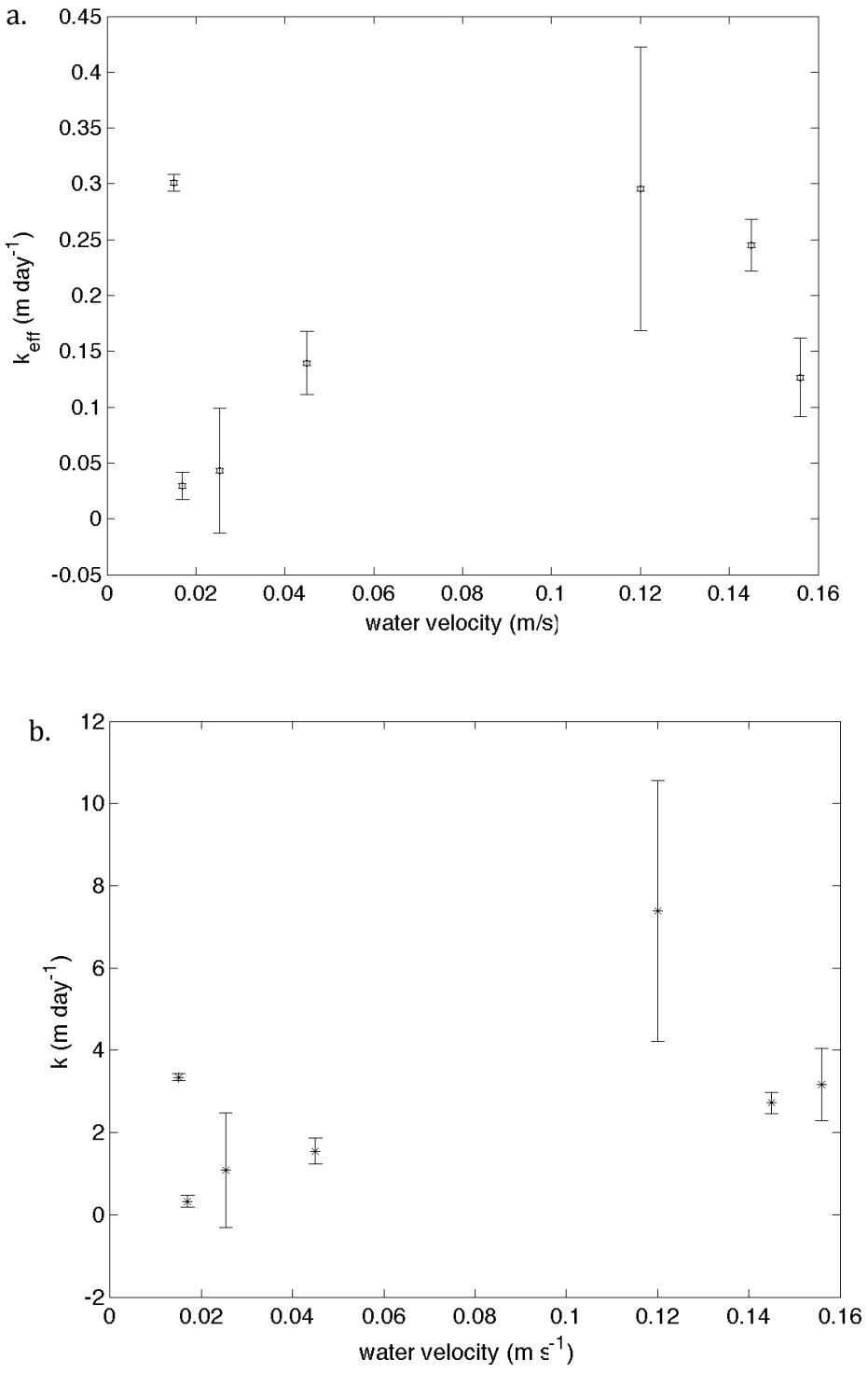

Figure 13. The mean water velocity plotted against a). k_{eff} and b). k. k is scaled by the amount of open water so that the lead size does not effect these values. No wind is blowing at the highest two water velocity measurements, but k and k_{eff} are increased, showing that some gas exchange results from the turbulence of the water current.

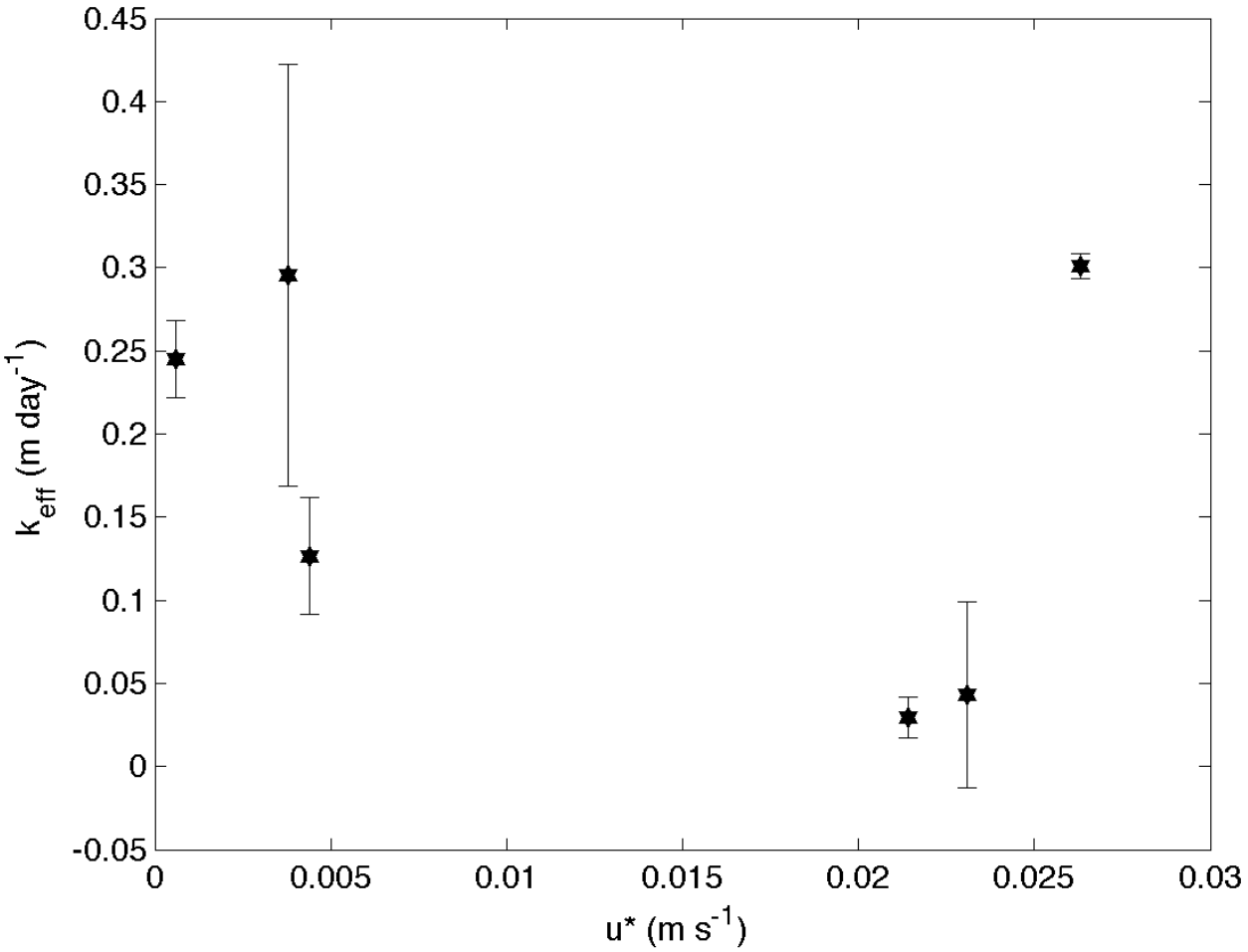

Figure 14. u_* plotted against k_{eff}. Low u_* values result from low wind conditions while high u_*'s result from high wind. It is clear that more than the shear at the surface is causing gas exchange, as some low shear (small u_*) conditions have high k_{eff}

REFERENCES

Ahn, J., Headly, M., Wahlen, M., Brook, E. J., Mayewski, P. A. and Taylor, K. C.: CO2 diffusion in polar ice: observations from naturally formed CO2 spikes in the Siple Dome (Antarctica) ice core, J. Glaciol., 54(187), 685–695, doi:10.3189/002214308786570764, 2008.

Arrigo, K. R. and van Dijken, G. L.: Interannual variation in air-sea CO2 flux in the Ross Sea, Antarctica: A model analysis, J. Geophys. Res. Oceans, 112, 3020, doi:10.1029/2006JC003492, 2007.

Bortkovskii, R. S.: Estimation of oxygen and carbonic acid diffusion through sea ice, Izv. Atmospheric Ocean. Phys., 48(5), 538–543, doi:10.1134/S0001433812040044, 2012.

Caldeira, K. and Duffy, P. B.: The Role of the Southern Ocean in Uptake and Storage of Anthropogenic Carbon Dioxide, Science, 287(5453), 620–622, doi:10.1126/science.287.5453.620, 2000.

Cox, G. F. N. and Weeks, W. F.: Equations for Determining the Gas and Brine Volumes in Sea Ice Samples,, J. Glaciol., 29(102), 306–316, 1983.

Else, B. G. T., Papakyriakou, T. N., Galley, R. J., Drennan, W. M., Miller, L. A. and Thomas, H.: Wintertime CO2 fluxes in an Arctic polynya using eddy covariance: Evidence for enhanced air-sea gas transfer during ice formation, J. Geophys. Res. Oceans, 116(C9), n/a–n/a, doi:10.1029/2010JC006760, 2011.

Fanning, K. A. and Torres, L. M.: 222Rn and 226Ra: indicators of sea-ice effects on air-sea gas exchange, Polar Res., 10(1), 51–58, doi:10.3402/polar.v10i1.6727, 1991.

Glover, D. M., Jenkins, W. J. and Doney, S. C.: Modeling Methods for Marine Science, Cambridge University Press, Cambridge ; New York., 2011.

Golden, K. M.: Brine percolation and the transport properties of sea ice, Ann. Glaciol., 33(1), 28–36, doi:10.3189/172756401781818329, 2001.

Gosink, T. A., Pearson, J. G. and Kelley, J. J.: Gas movement through sea ice, Nature, 263(5572), 41–42, doi:10.1038/263041a0, 1976.

Himmelblau, D. M.: Diffusion of Dissolved Gases in Liquids, Chem. Rev., 64(5), 527–550, doi:10.1021/cr60231a002, 1964.

Jähne, B., Heinz, G. and Dietrich, W.: Measurement of the diffusion coefficients of sparingly soluble gases in water, J. Geophys. Res. Oceans, 92(C10), 10767–10776, doi:10.1029/JC092iC10p10767, 1987.

Khatiwala, S., Primeau, F. and Hall, T.: Reconstruction of the history of anthropogenic CO2 concentrations in the ocean, Nature, 462(7271), 346–349, doi:10.1038/nature08526, 2009.

Khatiwala, S., Tanhua, T., Mikaloff Fletcher, S., Gerber, M., Doney, S. C., Graven, H. D., Gruber, N., McKinley, G. A., Murata, A., Ríos, A. F., Sabine, C. L. and Sarmiento, J. L.: Global ocean storage of anthropogenic carbon, Biogeosciences Discuss, 9(7), 8931–8988, doi:10.5194/bgd-9-8931-2012, 2012.

Loose, B., McGillis, W. R., Perovich, D., Zappa, C. J. and Schlosser, P.: A parameter model of gas exchange for the seasonal sea ice zone, Ocean Sci, 10(1), 17–28, doi:10.5194/os-10-17-2014, 2014.

Loose, B., McGillis, W. R., Schlosser, P., Perovich, D. and Takahashi, T.: Effects of freezing, growth, and ice cover on gas transport processes in laboratory seawater experiments, Geophys. Res. Lett., 36(5), n/a–n/a, doi:10.1029/2008GL036318, 2009.

Loose, B. and Schlosser, P.: Sea ice and its effect on CO2 flux between the atmosphere and the Southern Ocean interior, J. Geophys. Res. Oceans, 116(C11), n/a–n/a, doi:10.1029/2010JC006509, 2011.

Loose, B., Schlosser, P., Perovich, D., Ringelberg, D., Ho, D. T., Takahashi, T., Richter-Menge, J., Reynolds, C. M., Mcgillis, W. R. and Tison, J.-L.: Gas diffusion through columnar laboratory sea ice: implications for mixed-layer ventilation of CO2 in the seasonal ice zone: GAS DIFFUSION THROUGH COLUMNAR LABORATORY SEA ICE, Tellus B, 63(1), 23–39, doi:10.1111/j.1600-0889.2010.00506.x, 2011.

Marinov, I., Gnanadesikan, A., Toggweiler, J. R. and Sarmiento, J. L.: The Southern Ocean biogeochemical divide, Nature, 441(7096), 964–967, doi:10.1038/nature04883, 2006.

McNeil, C. and D'Asaro, E.: Parameterization of air–sea gas fluxes at extreme wind speeds, J. Mar. Syst., 66(1–4), 110–121, doi:10.1016/j.jmarsys.2006.05.013, 2007.

McPhee, M. G.: Turbulent heat flux in the upper ocean under sea ice, J. Geophys. Res. Oceans, 97(C4), 5365–5379, doi:10.1029/92JC00239, 1992.

Monteiro, P. M. S., Schuster, U., Hood, M., Lenton, A., Metzl, N., Olsen, A., Rogers, K., Sabine, C. L., Takahashi, T., Tilbrook, B., Yoder, J., Wanninkhof, R. and Watson, A.: A Global Sea Surface Carbon Observing System: Assessment of Changing Sea Surface CO2 and Air-Sea CO2 Fluxes, pp. 702–714, European Space Agency., 2010.

Moreau, S., Vancoppenolle, M., Zhou, J., Tison, J.-L., Delille, B. and Goosse, H.: Modelling argon dynamics in first-year sea ice, Ocean Model., 73, 1–18, doi:10.1016/j.ocemod.2013.10.004, 2014.

Morison, J. H., McPhee, M. G., Curtin, T. B. and Paulson, C. A.: The oceanography of winter leads, J. Geophys. Res. Oceans, 97(C7), 11199–11218, doi:10.1029/92JC00684, 1992.

Namiot, A. Y. and Bukhgalter, É. B.: Clathrates formed by gases in ice, J. Struct. Chem., 6(6), 873–874, doi:10.1007/BF00747111, 1965.

National Snow and Ice Data Center (NSIDC): http://nsidc.org/, last access: June 1, 2014.

Omar, A., Johannessen, T., Bellerby, R. G. J., Olsen, A., Anderson, L. G. and Kivimäe, C.: Sea-Ice and brine formation in Storfjorden: Implications for the Arctic wintertime air—sea CO2 flux, in The Nordic Seas: An Integrated Perspective, edited by Helgeange, T. Dokken, T. Furevik, R. Gerdes, and W. Berger, pp. 177–187, American Geophysical Union. [online] Available from: http://onlinelibrary.wiley.com/doi/10.1029/158GM12/summary (Accessed 12 June 2014), 2005.

Petrich, C. and Eicken, H.: Growth, Structure and Properties of Sea Ice, in Sea Ice, edited by D. N. Thomas and G. S. Dieckmann, pp. 23–77, Wiley-Blackwell. [online] Available from: http://onlinelibrary.wiley.com/doi/10.1002/9781444317145.ch2/summary (Accessed 5 June 2014), 2009.

Pilson, M. E. Q.: An introduction to the chemistry of the sea, Cambridge university press, Cambridge., 2013.

Rutgers van der Loeff, M. M., Cassar, N., Nicolaus, M., Rabe, B. and Stimac, I.: The influence of sea ice cover on air-sea gas exchange estimated with radon-222 profiles, J. Geophys. Res. Oceans, n/a–n/a, doi:10.1002/2013JC009321, 2014.

Stephens, B. B. and Keeling, R. F.: The influence of Antarctic sea ice on glacial–interglacial CO 2 variations, Nature, 404(6774), 171–174, doi:10.1038/35004556, 2000.

Stroeve, J. C., Markus, T., Boisvert, L., Miller, J. and Barrett, A.: Changes in Arctic melt season and implications for sea ice loss, Geophys. Res. Lett., 41(4), 2013GL058951, doi:10.1002/2013GL058951, 2014.

Takahashi, T., Feely, R. A., Weiss, R. F., Wanninkhof, R. H., Chipman, D. W., Sutherland, S. C. and Takahashi, T. T.: Global air-sea flux of CO2: An estimate based on measurements of sea–air pCO2 difference, Proc. Natl. Acad. Sci., 94(16), 8292–8299, 1997.

Takahashi, T., Sutherland, S. C., Wanninkhof, R., Sweeney, C., Feely, R. A., Chipman, D. W., Hales, B., Friederich, G., Chavez, F., Sabine, C., Watson, A., Bakker, D. C. E., Schuster, U., Metzl, N., Yoshikawa-Inoue, H., Ishii, M., Midorikawa, T., Nojiri, Y.,

Körtzinger, A., Steinhoff, T., Hoppema, M., Olafsson, J., Arnarson, T. S., Tilbrook, B., Johannessen, T., Olsen, A., Bellerby, R., Wong, C. S., Delille, B., Bates, N. R. and de Baar, H. J. W.: Climatological mean and decadal change in surface ocean pCO2, and net sea–air CO2 flux over the global oceans, Deep Sea Res. Part II Top. Stud. Oceanogr., 56(8-10), 554–577, doi:10.1016/j.dsr2.2008.12.009, 2009.

Top, Z., Martin, S. and Becker, P.: A laboratory study of dissolved noble gas anomaly due to ice formation, Geophys. Res. Lett., 15(8), 796–799, doi:10.1029/GL015i008p00796, 1988.

Torgersen, T., Top, Z., Clarke, W. B., Jenkins, W. J. and Broecker, W. S.: A new method for physical limnology-tritium-helium-3 ages: Results for Lakes Erie, Huron, and Ontario, Liminology Oceanogr., 22(2), 181–193, doi:10.4319/lo.1977.22.2.0181, 1977.

Vancoppenolle, M., Meiners, K. M., Michel, C., Bopp, L., Brabant, F., Carnat, G., Delille, B., Lannuzel, D., Madec, G., Moreau, S., Tison, J.-L. and van der Merwe, P.: Role of sea ice in global biogeochemical cycles: emerging views and challenges, Quat. Sci. Rev., 79, 207–230, doi:10.1016/j.quascirev.2013.04.011, 2013.

Wanninkhof, R.: Relationship between wind speed and gas exchange over the ocean, J. Geophys. Res. Oceans, 97(C5), 7373–7382, doi:10.1029/92JC00188, 1992.

Wanninkhof, R., Asher, W. E., Ho, D. T., Sweeney, C. and McGillis, W. R.: Advances in quantifying air-sea gas exchange and environmental forcing, Annu. Rev. Mar. Sci., 1 [online] Available from: http://www.vliz.be/en/imis?module=ref&refid=131247&printversion=1&dropIMIStitle=1 (Accessed 2 January 2014), 2009.

Wanninkhof, R., Ledwell, J. R., Broecker, W. S. and Hamilton, M.: Gas exchange on Mono Lake and Crowley Lake, California, J. Geophys. Res. Oceans, 92(C13), 14567–14580, doi:10.1029/JC092iC13p14567, 1987.

Weiss: Carbon dioxide in water and seawater: the solubility of a non-ideal gas, Mar. Chem., 2, 203–215, doi:10.1016/0304-4203(74)90015-2, 1974.

Appendix A: Error Propagation

When solving for k_{eff}, both the concentration of gas in the water (C_w) and air (C_a) are accounted for. Thus, the error of each of these values must be determined before determining the error in k_{eff}.

a. Determining error in C_w

The concentration of tracer in the water was determined by fitting a line to the GC measurements taken during each scenario and then adding back the concentration of tracer lost into the ice (determined from the finite difference model). Thus, the GC analytical error, the error of the line of best fit, and the finite difference model error are all important.

To determine the analytical error of the GC ($Var[C_{gc}]$), the variance of the duplicates taken during each sampling event was used. This variance was then propagated through the equation for the line of best fit in order to determine the variance of the fit ($Var[C_{fit}]$).

$$Var[C_{fit}] = Var[C_{gc} * m + b] \qquad \text{(A1)}$$

where m is the slope of the best fit line and b is the y-intercept. This equation becomes

$$Var[C_{fit}] = Var[C_{gc}] * m^2 \qquad \text{(A2)}$$

and is equal to the variance of the measured concentration of tracer in the water; C_w.

This value accounts for the gas lost to both the air and ice. The gas lost to the ice is added back to C_w, so the variance of the modeled concentration of tracer in the ice ($Var[C_{model}]$) must then be determined and added back to account for this addition.

Before calculating $Var[C_{model}]$ the variance of the diffusion coefficient ($Var[D]$) was determined from the square of the difference between the measured bulk concentration of tracer in the ice and the model estimates of the bulk ice concentration (C_{ice}) at a given instant in time.

Then, to determine $Var[C_{modeled}]$ we approximated the model flux of gas through the ice using the gas exchange equation

$$k = \frac{z}{dt}\ln(\frac{C_i}{C_f}) \qquad \text{(A3)}$$

since propagating the error through the finite difference model was not practical. In this equation, k is the gas transfer velocity, z is the ice thickness, dt is the time passed, C_i is the initial concentration of gas in the ice and C_f is the final concentration of gas in the ice. k is a velocity (m day^{-1}), it can be set to equal D/z, where D is the diffusion constant (cm^2 day^{-1}). Thus,

$$\frac{D}{z} = \frac{1}{dt}\ln(\frac{C_i}{C_f}) \qquad \text{(A4)}$$

and

$$C_f = C_i * e^{-D(\frac{dt}{dz})} \qquad \text{(A5)}$$

Thus

$$Var[C_f] = Var[C_i * e^{-D\left(\frac{dt}{dz}\right)}] \qquad \text{(A6)}$$

This is a non-linear equation, so to solve it we used

$$Var\left[C_f\right] = Var[D] * \left(\frac{\partial C_f}{\partial D}\right)^2 = Var[C_{ice}] = Var[C_{modeled}] \qquad \text{(A7)}$$

where (Glover et al., 2011)

$$\frac{\partial C_f}{\partial D} = -\frac{dt}{dz}C_i e^{-D\frac{dt}{dz}} \qquad \text{(A8)}$$

The final variance of the water concentration was determined by

$$Var[C_w] = Var\left[C_{fit}\right] + Var[C_{model}] \qquad \text{(A9)}$$

The value for $Var[C_w]$ calculated using error propagation through these equations was much smaller than the variance of the duplicates. $Var[C_{fit}]$ became very small when multiplied by the square of the slope of the line, which was tiny due to the small concentrations. $Var[C_{model}]$'s small size resulted from the vary small values of $Var[D]$. Because of this, $Var[C_w]$ was instead set to equal the variance of the duplicates.

b. Determining error in C_a

Air concentration of N_2O and SF_6 was measured in duplicate every 4 hours. The variance of the air concentration ($Var[C_a]$) was set equal to the variance of the duplicates measured during each scenario.

c. Determining error in k_{eff}

The final variance of the C_w and the variance of C_a were used to determine the variance of k_{eff} through propagation of error through the equation for k_{eff}:

$$Var[k] = Var[C_w]\left[\left(\frac{h}{dt}\left(\frac{1}{C_{wf} - C_a}\right)\right)^2 - \left(\frac{h}{dt}\left(\frac{1}{C_{wf} - C_a}\right)\right)^2\right]$$

$$-Var[C_a]\left[\left(\frac{h}{dt}\left(\frac{1}{C_{wf} - C_a}\right)\right)^2 - \left(\frac{h}{dt}\left(\frac{1}{C_{wf} - C_a}\right)\right)^2\right] \qquad \text{(A10)}$$

The final $Var[k]$ is less than 10% error for all tracers during all scenarios except scenario 4. The propagated error is also smaller than the standard error in k between individual gases for all scenarios (Table 3).